Czech Technical University in Prague
Faculty of Civil Engineering

The Department of Landscape Water Conservation
Environmental Engineering

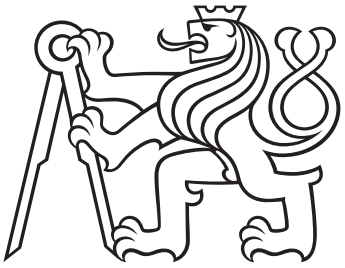

Analysis of surface temperature of substrate of an extensive green roof

DIPLOMA THESIS

Bc. Do Thi Mai Dung
2024

ČESKÉ VYSOKÉ UČENÍ TECHNICKÉ V PRAZE
Fakulta stavební
Thákurova 7, 166 29 Praha 6

ZADÁNÍ DIPLOMOVÉ PRÁCE

I. OSOBNÍ A STUDIJNÍ ÚDAJE

Příjmení: Do Jméno: Thi Mai Dung Osobní číslo: 484687

Zadávající katedra: K143

Studijní program: Stavební inženýrství

Studijní obor/specializace: Inženýrství životního prostředí

II. ÚDAJE K DIPLOMOVÉ PRÁCI

Název diplomové práce: Analýza povrchových teplot substrátu extenzivní vegetační střechy

Název diplomové práce anglicky: Substrate surface temperature analysis of an extensive green roof

Pokyny pro vypracování:
Cílem práce je experimentálně ověřit, jak se liší povrchové teploty substrátu zelené střechy v místech s vegetací a bez vegetace. V rámci práce budete provádět následující činnosti:

- Rešerše: Prostudujte dostupnou literaturu o metodách měření povrchových teplot půdy.
- Měření: Zvolte vhodné senzory a zařízení pro měření povrchových teplot substrátu v místech zelené střechy s vegetací a bez vegetace. Měřte v letním a podzimním období.
- Analýza: Zpracujte naměřená data statistickými metodami a porovnejte je s podpovrchovými a referenčními teplotami. Volitelně použijte jednoduchý model pro simulaci povrchových teplot.

Seznam doporučené literatury:
Hillel D., Introduction to environmental soil physics, Elsevier, 2003
Články v časopisech indexovaných v WOS.

Jméno vedoucího diplomové práce: doc. Ing. Michal Sněhota Ph.D.

Datum zadání diplomové práce: 5.10.2023 Termín odevzdání DP v IS KOS: 8.1.2024
Údaj uveďte v souladu s datem v časovém plánu příslušného ak. roku

Podpis vedoucího práce Podpis vedoucího katedry

III. PŘEVZETÍ ZADÁNÍ

Beru na vědomí, že jsem povinen vypracovat diplomovou práci samostatně, bez cizí pomoci, s výjimkou poskytnutých konzultací. Seznam použité literatury, jiných pramenů a jmen konzultantů je nutné uvést v diplomové práci a při citování postupovat v souladu s metodickou příručkou ČVUT „Jak psát vysokoškolské závěrečné práce“ a metodickým pokynem ČVUT „O dodržování etických principů při přípravě vysokoškolských závěrečných prací“.

Datum převzetí zadání Podpis studenta(ky)

Declaration

I declare that I have prepared my thesis independently under the supervision of doc. Ing. Michal Sněhota, Ph.D. and with the help of the mentioned sources of information.

In Prague 15. 01. 2024 .....

Bc. Do Thi Mai Dung

Acknowledgements

I would like to begin by expressing my profound gratitude to God, for His presence and support in each step of my academic journey. The strength and comfort He has provided have been the cornerstone of my perseverance.

I am also grateful to my family and friends for their encouragement, belief in my abilities and unwavering care.

I extend my heartfelt thanks to doc. Ing. Michal Sněhota, Ph.D., my supervisor, for the invaluable guidance, patience, and expertise.

Lastly, I would like to express a special thank to Czech Science Foundation of the Czech Republic (grant no. 22-25673S) and the Grant Agency of the Czech Technical University in Prague (SGS20/157/OHK1/3T/11) for financial support of the study.

Abstract

This study analyses the dynamic thermal behaviour of an experimental green roof, focusing on fluctuations in surface temperature and their correlation with environmental factors. Over a thirteen-week period, surface temperatures were monitored on both bare soil and vegetated section, and the influence of solar radiation on the roof's surface temperature was analyzed. The study aimed to determine temperature patterns, establish comparisons with subsurface temperatures, and conduct statistical analysis using a simple heat transfer model. The findings suggest that vegetation has a notable cooling impact, particularly in warm weather, but this effect decreases during periods of high temperatures. The study reveals the vulnerability of bare soil regions to temperature extremes and demonstrates the importance of green roofs in urban temperature regulation and the mitigation of urban heat islands. The predictive model used in the study generally aligned with actual temperature measurements, although it showed limitations during extreme high temperature conditions. The research suggests improvements in predictive modeling to better account for the complex reactions of green roof systems to various external factors. In conclusion, the study provides insights into the design and management of green roofs, highlighting the need for extensive vegetation to control microclimates and the consideration of seasonal variations. The results contributes to improved understanding of green roof thermal dynamics, and eventually help in the creation of more efficient green infrastructure.

Abstrakt

Tato studie se zabývá analýzou teplotního chování experimentální zelené střechy s důrazem na povrchové teploty a její interakci s environmentálními faktory. Během třinácti týdenního období byly monitorovány povrchové teploty na holé půdě i na ozeleněné části střechy, společně s posouzením vlivu slunečního záření na vývoj povrchové teploty. Cílem studie bylo změřit vývoj povrchové teploty, provést srovnání s teplotami pod povrchem a aplikovat statistickou analýzu pro vyhodnocení experimentu a prostřednictvím jednoduchého modelu simulovat přenos tepla. Výsledky ukazují, že vegetace na střeše má výrazný chladicí efekt, zejména během teplého počasí, avšak tento efekt je redukován v obdobích vysokých teplot. Studie také poukazuje na zvýšenou citlivost holých půdních oblastí vůči teplotním extrémům. Použitý predikční model se většinou shodoval s reálnými teplotními měřeními, ale vykazoval omezení během extrémních povětrnostních podmínek. Výzkum navrhuje modifikaci predikčního modelu pro lepší reprezentaci komplexních reakcí zelených střešních systémů na různé externí vlivy. Závěrem studie nabízí poznatky pro návrh a správu zelených střech, zdůrazňuje potřebu rozsáhlé vegetace pro efektivní kontrolu mikroklimatu a upozorňuje na význam zahrnutí sezónní variability. Výsledky dílčím způsobem přispívají k hlubšímu porozumění tepelné dynamice zelených střech a posílení jejich role v rozvoji efektivní zelené infrastruktury.

Contents

1 Introduction **11**

2 Objectives **12**

3 Literature research **13**
3.1 Theory of soil temperature and heat flux in soil 13
3.2 Methods for measuring soil surface temperature 20
3.3 Model of behaviour of surface temperature 26

4 Practical part **28**
4.1 Temperature sensors 28
4.2 Laboratory work 31
4.3 Experiment on green roof 32
4.4 Temperature sensors installation 35
4.5 Measured data pre-processing and analysis 36

5 Results **39**
5.1 Laboratory work 39
5.2 Measurement on the experimental green roof 41

6 Discussion **63**
6.1 Laboratory experiments 63
6.2 Measurement on the experimental green roof 64

7 Conclusion **69**

References **70**

8 Appendix A - Matlab script **75**

List of Figures

1 Scheme of heat transfer mechanism . . . 13
2 Scheme of radiative heat transfer . . . 14
3 The four forms of heat transfer . . . 16
4 Thermal properties of common components in soil . . . 17
5 Idealized daily fluctuation of surface soil temperature . . . 19
6 Idealized variation of soil temperature with time for various depths . . . 19
7 Types of temperature sensors . . . 20
8 Radiation thermometer . . . 21
9 Thermal imaging camera . . . 21
10 Thermistors . . . 23
11 Thermocouples . . . 23
12 Resistance temperature detector . . . 23
13 IC temperature sensor . . . 23
14 Fiber optic temperature sensor . . . 24
15 The circuit board and a finished array . . . 25
16 Scheme of the model of surface temperature on bare soil . . . 26
17 Energy flow for bare soil . . . 27
18 The 109 Temperature Probe . . . 28
19 Polystyren cube . . . 29
20 Alumunium plate and Pt100 adhesive temperature sensor . . . 29
21 Pt100 temperature sensor glued to aluminum plate . . . 29
22 Photograph of both temperature sensors used in the study . . . 29
23 Thin stainless steel probe on the iced substrate . . . 31
24 Temperature sensor with aluminium plate and thin stainless steel probe on the iced substrate . . . 31
25 Map of the Czech Republic showing the location of UCEEB . . . 32
26 UCEEB with marked location of the experiment . . . 32
27 Location of the experiment . . . 33
28 Scheme of the green roof test bed . . . 34
29 Experimental green roof area . . . 34
30 Installed sensors on bare soil . . . 35
31 Photograph of sensors installed on the vegetated surface . . . 35
32 Location of temperature sensors on the test green roof . . . 35
33 Simple box plot with . . . 36
34 Graph of settling temperature sensors on frozen substrate . . . 39
35 Graph of settling temperature sensors on heated substrate . . . 40
36 Box plot of temperatures measured on the part of experimental green roof with bare soil . . . 42
37 Box plot of temperatures measured on the part of experimental green roof with vegetation . . . 43
38 Box plot of upward longwave radiation . . . 44

39 Box plot of upward shortwave radiation 45
40 Box plot of downward longwave radiation 46
41 Box plot of downward shortwave radiation 47
42 Box plot of net radiation 48
43 Temperatures of bare soil, area with vegetation, subsurface of substrate and temperatures in 2m and 5cm above the green roof 49
44 Total weekly rain amounts 49
45 Relationship between surface temperature of bare soil, surface temperature of an area with the vegetation and air temperature 51
46 Relationship between temperature of bare soil and part with the vegetation with net radiation 53
47 Relationship between temperature of bare soil and part with the vegetation with downward shortwave radiation 55
48 Relationship between temperature of bare soil and part with the vegetation with temperature change 57
49 Comparison of measured and modeled soil surface temperature in WEEK 1 (highest rainfall) 59
50 Comparison of measured and modeled soil surface temperature in WEEK 6 (no rainfall) 60
51 Comparison of measured and modeled soil surface temperature in WEEK 3 (highest temperature) 61
52 Comparison of measured and modeled soil surface temperature in WEEK 13 (lowest temperature) 62

List of Tables

1 Estimated variables 38
2 Overview of individual weeks of the study 41

1 Introduction

In recent years, the concept of green infrastructure has emerged as a beacon of sustainable urban development [Tzoulas et al., 2007], revolutionizing the way we conceive and interact with our built environments [Pauleit et al., 2019]. At the forefront of this movement lies the extensive green roof—a marvel of ecological design that not only adorns city skylines but also serves as a dynamic solution to pressing urban challenges [Oberndorfer et al., 2007]. A pivotal aspect in understanding and optimizing the efficiency of these green roofs is the analysis of surface temperature of bare and vegetated substrate [Niachou et al., 2001]. This analysis serves as a linchpin in comprehending the thermal behavior of these rooftop landscapes, offering invaluable insights into their performance and impact. The thermal behavior is influenced by various factors, including solar radiation, the angle of the land, the amount of water present, the vegetation covering, and the albedo [Sailor, 2008]. Soil temperature measurement is necessary as a consequence. The temperature of the soil has an impact on various processes such as photosynthesis, respiration, transpiration, water potential of the soil, soil translocation, and microbial activity [Asshoff et al., 2006].

Delving into the green roof's temperature allows us to decipher its role in mitigating the urban heat island effect, regulating building temperatures, and enhancing energy efficiency [Santamouris, 2014]. By closely monitoring these temperatures, we gain a nuanced understanding of how green roofs function as natural insulators, providing cooling benefits in scorching summers and contributing to heat retention during colder months [Fioretti et al., 2010]. The temperature has an impact on various processes occurring in the soil and the soil ecology.

Knowledge of substrate surface temperature, can help to unravel the intricate mechanisms behind green roofs' ability to reduce energy consumption, mitigate environmental stressors, and create conducive living spaces [Yu et al., 2008]. It reveals key mechanisms such as improved building insulation for energy efficiency, evapotranspiration cooling, and the albedo effect, which reflect sunlight and reduce heat absorption.This exploration not only informs better design strategies but also empowers us to harness the full potential of green roofs in shaping resilient and sustainable cities for generations to come [Berardi et al., 2014].

2 Objectives

The aim of the thesis is to determine the surface temperature behavior on the substrate of an experimental green roof. The objective is to perform a comparative analysis of temperatures recorded on bare soil and a sections of vegetation within the same experimental green roof. The secondary objective is to compare these temperatures with the subsurface temperature of the green roof and the ambient temperature. The additional objective is to monitor other factors that influence the behavior of temperature. Lastly, the aim of the thesis is to statistically analyze the results and attempt simulation of the surface temperature using a simple model.

3 Literature research

3.1 Theory of soil temperature and heat flux in soil

The soil temperature, both its instantaneous value and its temporal and spatial variations, plays a crucial role in influencing the rates and directions of soil physical processes, as well as the exchange of energy and mass with the atmosphere [Hillel, 2003]. The temperature controls the processes of evaporation and aeration, as well as the kind and speed of chemical reactions occurring in the soil. Soil temperature significantly impacts various biological activities, including seed germination, seedling emergence and growth, root development, and microbial activity [Hillel, 2014, Stevenson, 1979].

The temperature of the soil fluctuates due to changes in the radiant, thermal, and latent energy exchange processes, which largely occur through the soil surface. The relevant soil parameters encompass the specific heat capacity, thermal conductivity, and thermal diffusivity, along with the internal sources and sinks of heat that are active at any given time [Hillel, 2003].

Mechanism of heat transfer

The transfer of energy occurs through three primary modes: radiation, convection, and conduction (Figure 1).

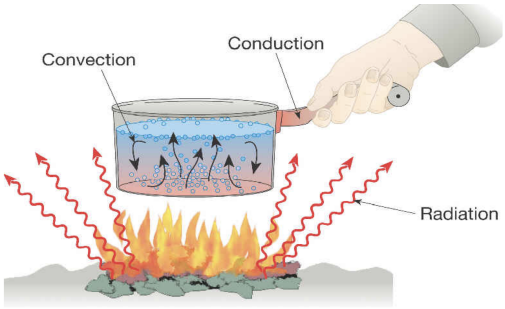

Figure 1: Scheme of heat transfer mechanism (adapted from [Johnston, 2020])

Radiation is the release of energy as electromagnetic waves from any object with a temperature above absolute zero [Hillel, 2003]. The Stefan-Boltzmann law is often formulated:

$$J_t = \varepsilon \sigma T^4 \quad [1]$$

where T is temperature [K], ε is the emissivity coefficient and σ is the Stefan-Boltzmann constant with numerical value of 5,6705119.10^{-8} W/m^2K^4

[Young et al., 2014].

The absolute temperature is a determining factor in the distribution of radiated energy's wavelength. According to Wien's rule, the wavelength at which radiation intensity is highest λ_m is inversely proportional to the absolute temperature [Hillel, 2014]:

$$\lambda_m = \frac{2900}{T} \quad [2]$$

where λ_m is in micrometers.

Planck's law describes the relationship between radiative intensity and wavelength and temperature [Hillel, 2014]:

$$E_\lambda = C_1 \lambda^{-5} \left[\exp\left(\frac{C_2}{\lambda T} \right) - 1 \right] \quad [3]$$

where E_λ is energy flux emitted in a given wavelength range, C_1 and C_2 are constants.

The average soil surface radiation emitted by the soil is 300 K, with a peak intensity occurring at a wavelength of 10 μ_m and a range of wavelengths ranging from 3 μ_m to 50 μ_m. Figure 2 shows the scheme of radiation heat transfer. The sun emits radiation at a temperature of 6000 K, which consists of visible light, infrared radiation, and ultraviolet radiation [Hillel, 2003]. The solar spectrum that reaches the Earth is referred to as short-wave radiation, while the Earth's radiation is characterized by its low overlap and is known as long-wave radiation [Stevenson, 1979].

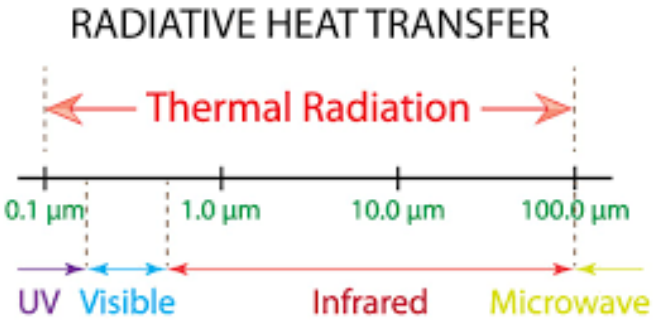

Figure 2: Scheme of radiative heat transfer (adapted from [Doe, 2024])

Convection, the second mechanism of energy transfer, entails the motion of a mass that carries heat, such as ocean currents and atmospheric winds [Hillel, 2003]. A more relevant example in the context of soil physics would involve the absorption of heated water into a soil that is initially at a lower temperature. The mechanism of convective heat transfer is complicated, and it requires coupled modeling of heat and water fluxes [Young et al., 2014, Stevenson, 1979, Votrubova et al., 2012] .

Conduction, the third mechanism of energy transfer, refers to the transmission of heat within an object by the movement of its interior molecules [Hillel, 2003]. Heat transfer only occurs between areas with different temperatures, and the heat always shifts from a higher temperature to a lower temperature [Young et al., 2014]. Temperature, representing kinetic energy in a body's molecules, transfers kinetic energy through collisions between fast-moving molecules. Heat conduction and diffusion aim to equalize the distribution of a substance, with heat conduction working to equalize temperature within an object, similar to how diffusion spreads mixture composition evenly over time [Stevenson, 1979, Hillel, 2014].

Fourier's law, the basic principle of heat conduction, asserts that heat flows through a uniform body in the direction of the temperature gradient and is directly proportional to it [Hillel, 2003]. The law is expressed by the equation:

$$q_h = -\kappa \nabla T \quad [4]$$

where q_h is the thermal flux, κ is thermal conductivity and ∇T is the spatial gradient of temperature T.

Apart from the three ways of energy transmission mentioned, there exists a combined process that can be identified as a fourth mode, specifically, **latent heat** transfer [Hillel, 2003]. An exemplary instance is the process of distillation, which encompasses the heat-absorbing phase of evaporation, succeeded by the convective or diffusive motion of the vapor, and culminating in the heat-releasing phase of condensation. An analogous process can also take place during the transition between ice and liquid water in soils that experience cycles of freezing and thawing [Stevenson, 1979, Hillel, 2014].

Heat transfer in soil is of major biological significance. The energy balance not only controls soil temperature, but also has a significant impact on the moisture content [Berardi et al., 2014]. The temperature of the soil is essential for the process of photosynthesis in green plants and the absorption of nutrients. It influences the speeds at which organisms process energy and can act as a signal for daily and seasonal behavioral patterns in a range of organisms, including fungi, bacteria, and insects [Stevenson, 1979]. The Figure 3 shows all four forms of heat transfer.

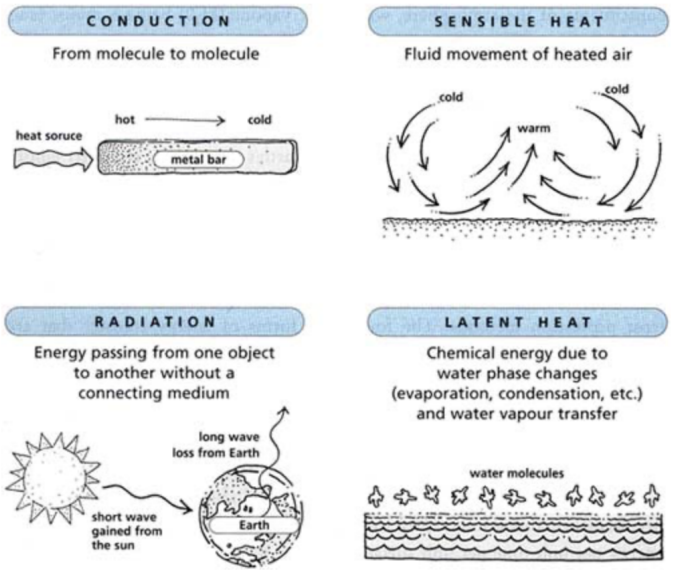

Figure 3: The four forms of heat transfer (adapted from [Food and Agriculture Organization of the United Nations, 2024])

Energy balance for bare soil

The radiation balance of an exposed surface, which can be expressed as follows [Van Bavel and Hillel, 1976]:

$$J_n = (J_s + J_a)(1 - \alpha) + J_{li} - J_{lo} \quad [5]$$

where J_n represents the net radiation, which is the total amount of radiant energy fluxes received minus the amount emitted. J_s is the direct short-wave radiation from the sun, J_a is the diffuse short-wave radiation from the atmosphere (sky), $J_l i$ is the incoming long-wave radiation from the sky, $J_l o$ is the outgoing long-wave radiation emitted by the soil and α represents the albedo or reflectivity coefficient, which is the fraction of incoming short-wave radiation that is reflected by the soil surface instead of being absorbed. In the current context, we will ignore all terms that are not related to the soil, specifically J_s, J_a, and $J_l i$.

The albedo α is an important feature of soil surfaces, which can vary considerably within the range of 0.1–0.4. This variation depends on the soil's inherent color (whether it is dark or light), the roughness of the surface, and the angle at which the incoming radiation strikes the surface [Sellers, 1965]. The albedo in the near term is also influenced by the varying moisture levels of the uncovered soil [Jackson et al., 1974]. As the soil becomes less moist, its surface becomes more even; as its color becomes more intense, its albedo increases [Graser and Van Bavel, 1982]. The albedo can be altered to some degree through various surface treatments, including as tillage and mulching [Hillel, 2003].

Soil thermal properties

The main thermal characteristics of soil are the heat capacity, the thermal conductivity and diffusivity [Horton and Ochsner, 2011].

Material	Density (kg/m^3)	Heat capacity (kJ/kg K)	Thermal conductivity (W/m K)	Thermal diffusivity (m^2/s) × 10^{-7}
Air (10 °C)	1.25	1.000	0.0026	0.21
Water (25 °C)	999.87	4.200	0.56	1.43
Water vapor (1 atm, 400 K)	–	1.901	0.016	233.8
Ice (0 °C)	917	2.040	2.25	12
Quartz	2,660	0.733	8.40	43.08
Granite	2,750	0.890	1.70–4.00	~12
Gypsum	1,000	1.090	0.51	4.7
Limestone	2,300	0.900	1.26–1.33	~5
Marble	2,600	0.810	2.80	13
Mica	2,883	0.880	0.75	2.956
Clay	1,450	0.880	1.28	10
Sandstone	~2,270	0.710	1.60–2.10	10–13

Figure 4: Thermal properties of common components in soil (adapted from [Tillman, 2015])

The volumetric **heat capacity** of soil C is the measure of the change in heat content per unit change in temperature for a certain volume. Volumetric heat capacity indicates a linear relationship with soil water content, in contrast to thermal conductivity [Fortin, 1993, Horton and Ochsner, 2011]. Therefore, C is influenced by the composition of the soil's solid phase (including mineral and organic components), as well as by bulk density and soil wetness [Hillel, 2014].

To estimate the value of C, one can calculate the sum of the heat capacities of the different components, taking into account their respective volume portions [De Vries, 1952]:

$$C = \sum (f_{si} C_{si} + f_w C_w + f_a C_a) \quad [6]$$

where f represents the volume fraction of each phase: solid (marked as s), water (w), and air (a). The solid phase consists of several components denoted by the subscript i, including different minerals and organic matter. The symbol $\sum$ is the summation of the products of their respective volume fractions and heat capacities. The C value for water, air, and each component of the solid phase is calculated by multiplying the respective density by the specific heat per unit mass (i.e., $C_w = \rho_w c_{mw}$).

Thermal conductivity, denoted by κ, is the measure of heat transfer across a specific area of a conducting object within a specific time period, given a specific temperature difference. The thermal conductivities of specific soil components show

significant variations, as illustrated in the Figure 4. Therefore, the overall thermal conductivity of a soil, which is calculated by averaging the values over a large area, is influenced by its mineral composition, organic matter content, and the proportions of water and air present [De Vries, 1952, De Vries and van Wijk, 1963].

The thermal conductivity of air is significantly lower than that of water or solid materials, causing a low thermal conductivity. The ratio of water to air is always changing, causing to be time-varying. The composition of soil is frequently uneven, resulting in κ being dependent on both depth and time. Temperature variations likewise impact it, but under typical circumstances, it is disregarded. The thermal conductivity of soil is influenced by factors such as the mineral content, particle sizes, and configurations [Hillel, 2014, Hillel, 2003].

The soil **thermal diffusivity** is defined as the ratio of the thermal conductivity and the volumetric heat capacity. It is a measure of the speed at which heat is transferred through the soil by conduction. High thermal diffusivity in soil results in quick transmission of temperature changes. The soil's thermal diffusivity is affected by all the factors that impact thermal conductivity and heat capacity. Thermal diffusivity is less affected by soil water content compared to thermal conductivity and volumetric heat capacity. The thermal diffusivity is a valuable characteristic for comprehending and simulating soil temperatures [De Vries, 1952, De Vries and van Wijk, 1963].

Thermal regime of soil profiles

The soil temperature in nature constantly varies due to the dynamic meteorological conditions at the interface between the soil and the atmosphere. This system is regulated by a consistent and repeating cycle of days, nights, summers, and winters. However, it is also impacted by sporadic and unpredictable events such as cloud cover, extreme cold spells, heavy rainstorms, snowstorms, and periods of drought. The variability of soil qualities, including reflectivity, heat capacity, and thermal conductivity, along with factors such as geographic location, vegetative cover, and human management, make it difficult to define the thermal characteristics of soil profiles [Hillel, 2003, Hillel, 2014].

A mathematical model (Figure 5) to describe varying temperature in nature suggests that soil temperature fluctuates in a regular pattern over time, resembling a pure harmonic function with an average value as its central point. This method, when combined with field data, can provide a more comprehensive understanding and forecast of a soil's thermal conditions [Hillel, 2003, Hillel, 2014]:

$$T(0,t) = T_{\text{ave}} + A_0 \sin \omega t \qquad [7]$$

where $T(0,t)$ represents the temperature at the soil surface (z = 0) as a function of time t. T_{ave} is the average temperature of both the surface and the entire profile. A_0 is the amplitude of the temperature variation at the surface (difference between

the maximum or minimum temperature and the average temperature). ω is the radial frequency, defined as 2π multiplied by the actual frequency.

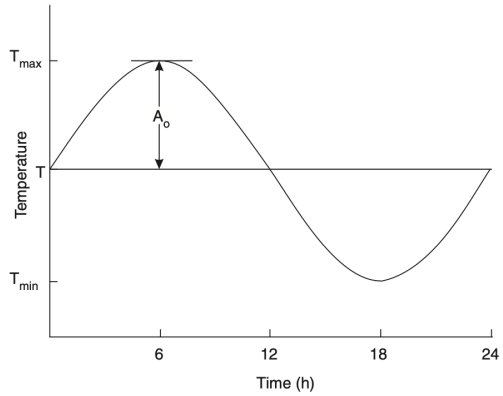

Figure 5: Idealized daily fluctuation of surface soil temperature (adapted from [Hillel, 2003])

The last formula is the boundary condition for z equals zero. To simplify the matter, let's assume that at an infinite depth (z = ∞), the temperature remains constant and is denoted as T_{ave}. In these conditions, the temperature at any given depth z can be expressed as a sinusoidal function of time, as illustrated in Figure 6 [Hillel, 2003, Hillel, 2014]:

$$T(z,t) = T_{\text{ave}} + A_z \sin(\omega t + \phi(z)) \qquad [8]$$

where A_z is the amplitude at depth z. Both A_z and $\phi(z)$ are functions of z.

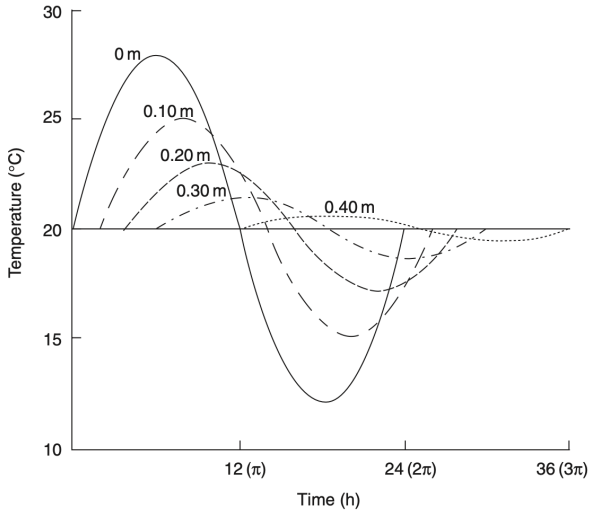

Figure 6: Idealized variation of soil temperature with time for various depths (adapted from [Hillel, 2003])

3.2 Methods for measuring soil surface temperature

Temperature sensors are employed to gauge the surface temperature of the soil and can be categorized into non-contact and contact sensors (Figure 7).

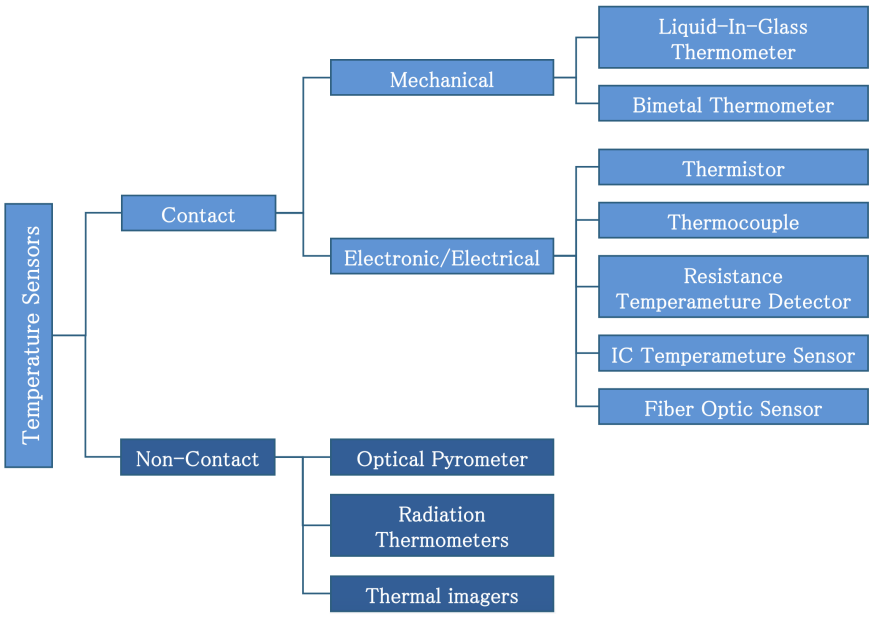

Figure 7: Types of temperature sensors

Non-contact temperature sensors

A non-contact temperature sensor employs a technology that enables the measurement of an object's temperature without physical contact, eliminating the need for direct surface contact. Non-contact temperature sensors function by quantifying the quantity of infrared radiation discharged by an object [Mukhopadhyay, 2022]. The primary benefits of non-contact sensors lie in their precision, rapidity, and adaptability. Thermal sensors have the capability to remotely gauge temperature, rendering them well-suited for dangerous settings and for quantifying exceedingly elevated temperatures [LambdaGeeks, 2023]. The main disadvantage of non-contact sensors is their inferior precision compared to contact sensors. Moreover, they are susceptible to inaccuracies caused by ambient radiation and might be obstructed by water droplets, dust, or debris. Also the visibility of the soil surface may be impeded by another surface (vegetation), potentially compromising the legitimacy of measurements [Gill, 2023]. There exist three categories of non-contact sensors.

Optical pyrometers consist of an optical system and a detector. The optical system concentrates the radiation onto the detector, enabling the measurement of temperature. They are especially effective in high-temperature environments like industrial furnaces, kilns, and for measuring the surface temperature of molten materials. Their non-contact measurement method is crucial in hazardous environments where direct contact is impossible or too dangerous [Kuphaldt, 2023].

Radiation thermometers (Figure 8) measure temperature variations by evaluating the radiation emitted by an object. These tools are highly beneficial in industrial settings for the purpose of monitoring heat treatment processes or chemical reactions, particularly in cases where the detection of temperature gradients is of critical importance [Kuphaldt, 2023].

Thermal imagers (Figure 9) share similarities to radiation thermometers. Nevertheless, they are capable of computing a two-dimensional area instead of determining temperature using a specified point on an object's surface [Davey, 2023]. They are highly beneficial in a wide range of applications, including construction inspections and agricultural monitoring. These devices are capable of detecting thermal energy loss in insulation, identifying excessive heat in electrical systems, and evaluating soil temperatures or crop health [Edwards, 2023].

Figure 8: Radiation thermometer (adapted from [MISUMI, 2024])

Figure 9: Thermal imaging camera (adapted from [EnnoLogic, 2023])

Contact temperature sensors

A contact temperature sensor is based on the idea that when it physically touches an object, it detects the temperature by conduction and generates a signal to regulate the desired temperature of a process [Mukhopadhyay, 2022]. Contact sensors offer significant benefits in terms of their exceptional accuracy and precision. Furthermore, they are impervious to background radiation and have a lower probability of being obstructed by dust or dirt. The primary drawbacks of contact sensors are the inherent logistical constraints associated with physically touching the object of interest and have the potential to sustain damage. Repairing or replacing parts of a larger mechanism can be costly and require specialized technical knowledge. [Woolf, 2023]. The contact-type temperature sensors can be classified into two primary categories: mechanical sensors and electronic (electrical) sensors [Mukhopadhyay, 2022].

A mechanical-type temperature sensor refers to a device that generates a signal by converting mechanical motion caused by a change in temperature. This signal can be observed through a visible scale or by activating or deactivating an electrical circuit loop. There are two types of them: **liquid-in-glass thermometer** and **bimetal thermomether** [Mukhopadhyay, 2022].

Electronic sensors are divided into five categories - thermistors, thermocouples, resistance temperature detectors, IC temperature sensors and fiber optic temperature sensor.[Mukhopadhyay, 2022].

Thermistors (Figure 10) detect the electrical resistance of a semiconductor substance when exposed to varying temperatures. The electrical resistance of the material is monitored by the thermistor, which changes when the temperature of the material fluctuates [Mukhopadhyay, 2022]. A thermistor is a THERMally sensitive resISTOR [Fallis, 2013]. The resistance can be categorized as either positive temperature coefficient resistance (PTCR) or negative temperature coefficient resistance (NTCR) [Ramos et al., 2012]. The main advantages of employing thermistors include large resistance variations with temperature, availability in a wide range of resistances, no need for reference junctions, low impact on ambient conditions, small size, and mechanical toughness. Thermistors offer possible benefits such as increased temperature capabilities, uncomplicated design, and affordability [Aniley et al., 2017]. Researchers aspire to construct lead-free or low-quantity lead thermistors due to its potential harm to individuals and the environment [Wuest, 2013].

Thermocouples (Figure 11) measure the electrical potential produced when two different metals are connected [Mukhopadhyay, 2022]. The thermocouple monitors the electrical current that is generated due to the temperature differential between the two metal wires. The energy balance and consequent temperature measurements may be incorrect due to the impact of wind and rain, which frequently displace

thermocouples during field operations [Ham and Senock, 1992].

RTDs (Figure 12), or **Resistance Temperature Detectors**, measure temperature by assessing the resistance of a wire when subjected to varying temperatures. The electrical resistance of the wire is measured by the RTD, which varies in response to variations in the wire's temperature [Mukhopadhyay, 2022]. The usage of platinum sensors is predominantly favored because to its reliable response, enduring stability, and robustness [Fallis, 2013]. One drawback is the high cost [Mukhopadhyay, 2022].

Figure 10: Thermistors (adapted from [Systems, 2023])

Figure 11: Thermocouples (adapted from [Thermo-Probes, 2023])

Figure 12: Resistance temperature detector (adapted from [Sensors, 2023])

Figure 13: IC temperature sensor (adapted from [Halim, 2017])

An **IC temperature sensor** (Figure 13) is a type of integrated circuit temperature transducer that generates an output current that is directly proportional to the absolute temperature [Omega Engineering, 2023]. The sensor package is compact, possessing a minimal thermal mass and a rapid response time. IC sensors are the only one which exhibit linear transfer functions. This means that the relationship between temperature and the physical parameter being measured (such as resistance or voltage output) is linear [Feteira, 2009].

Fiber optic temperature sensors operate on the principle that the band-gap of Gallium Arsenide (GaAs), a semiconductor, varies predictably with temperature. Light transmitted through a fiber optic cable to the GaAs sensor is partially absorbed and reflected, with the spectrum of the reflected light indicating the temperature. These sensors are direct contact but are not subject to drift or recalibration. Advantages include their immunity to electromagnetic interference, high voltage, and explosive environments, making them suitable for harsh conditions. Disadvantage includes the need for specialized equipment for signal interpretation [Rugged Monitoring, 2019].

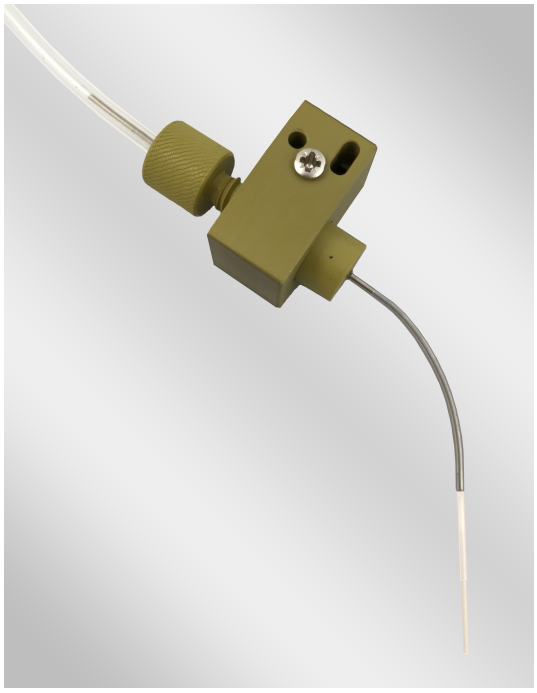

Figure 14: Fiber optic temperature sensor (adapted from [Solutions, 2023])

Several studies have attempted to adapt temperature sensors for hydrological experiments. A thermistor (10K ohm, NTC, I 10%, 135-303 F SG-J01, Honeywell, Morristovon, NJ) was encased in fiberglass and epoxy resin, with the inclusion of two carbon fiber strips, in order to enhance the rigidity over the entire length of the array, as demonstrated in a particular research investigation (Figure 15). The resulting gadget exhibited durability, rigidity, and water resistance. The sensor was positioned parallel to the soil surface. The researchers have determined that the array's sturdy structure enables it to be inserted directly into the soil, and the calibration procedure used guarantees precise temperature measurements [Wuest, 2013].

Figure 15: The circuit board and a finished array (adapted from [Wuest, 2013])

In another study [Ramos et al., 2012], a Pt100 temperature sensor (Pt100, Tiny talk, Orion) was employed. The sensor was positioned precisely at the midpoint of a square aluminum plate with strong thermal conductivity, measuring 10x10x0.5 cm. Simultaneously, the measurement of this device and the GTS - pyrometer (located 1.6 m above the surface) was being conducted in the same experimental area. Upon analyzing the data, it is determined that the average temperature variation during the night is 0.3 °C, whereas the average temperature variation during the day is 0.8 °C.

3.3 Model of behaviour of surface temperature

Simplified heat transfer model (Figure 16), which is open-source, was introduced by [Hong and Utzinger, 2021] to estimate the surface temperature of a green roof. This model takes into account the green roof materials and climate data as inputs and aims to minimize uncertainties related to radiation, convection, and evaporation effects.

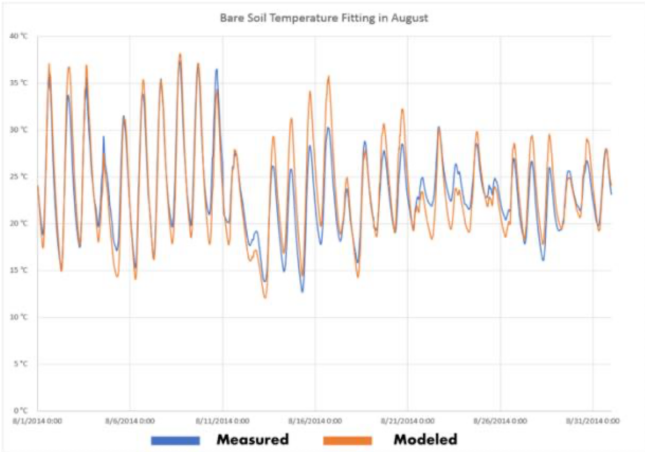

Figure 16: Scheme of the model of surface temperature on bare soil (adapted from [Hong and Utzinger, 2021])

Mathematical models facilitate the development of simulation programs that study the effectiveness of green roofs in saving energy and water retention [Hong and Utzinger, 2021]. A green roof's mathematical model involves two components: the energy balance model and the mass balance model. The heat and mass flow on green roofs is bound to the Law of Conservation of Energy and Mass:

$$\text{Input} - \text{Output} = \text{Energy or mass storage} \qquad [9]$$

In the energy balance model the heat transfer methods include solar radiation, sky radiation, heat convection, heat conduction and heat storage in the soil. In the mass balance model which is also the water balance, the water flows involve precipitation, evapotranspiration, condensation, drainage and retention. The energy flow on a green roof surface is affected by solar radiation, sky radiation, heat conduction, heat convection, and evaporation [Sailor, 2008]. Evaporation describes the process of water vaporizing and converting into vapor, which involves the release or absorption of latent heat.

Onsite analyzing revealed considerable variations in surface temperatures between bare soil and surfaces covered with vegetation. Consequently, it is necessary to create distinct energy balancing models for both a bare soil and a green roof with vegetation [Hong and Utzinger, 2021].

Bare Soil Energy Balance: Surface Temperature

The Figure 17 illustrates the energy fluxes in the bare soil in simple conceptual model. The bare soil surface absorbs solar radiation, exchanges radiation with the sky, transfers heat by convection with the surrounding air, and then conducts the heat downwards to the soil and nearby buildings. Additionally, heat is transferred to the soil through the process of heat conduction [Hong and Utzinger, 2021].

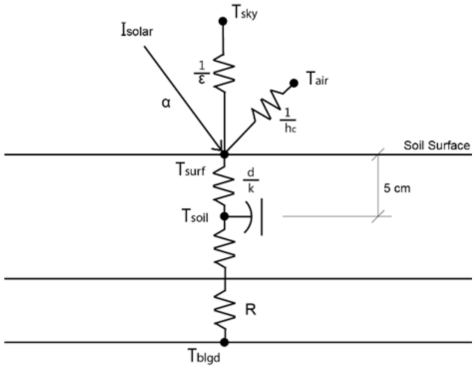

Figure 17: Energy flow for bare soil (adapted from [Hong and Utzinger, 2021])

4 Practical part

This chapter provides a detailed description of the temperature sensors used for the experiment, the laboratory testing procedures employed, and the following testing of the sensors on the green roof. It also explains how the experiment is set up on the test bed, how it is evaluated, and how the data is modeled afterwards.

4.1 Temperature sensors

Thin stainless steel probe

The thin stainless steel probe (Figure 18), known as The 109 Temperature Probe (T109, Campbell Scientific Logan, UT, USA) [Campbell Scientific, 2022], utilizes a high-quality thermistor to precisely measure temperature in various mediums such as air, soil, and water. Designed for durability and accuracy, it seamlessly connects with the majority of Campbell Scientific data loggers, offering versatility in environmental monitoring and research applications [Campbell Scientific, 2024].

The probe's survival range spans from -50 °C to 100 °C, making it ideal for a wide range of climatic conditions, while its measuring range extends from -50 °C to 70 °C, ensuring reliable data collection in extreme temperatures. The probe has a compact and subtile design with a length of 10.4 cm and a diameter of 0.762 cm, facilitating easy integration into various setups. Additionally, the probe features a fast response time, which is crucial for detecting rapid temperature changes, and it is equipped with a shield to reduce radiative heating effects, enhancing the accuracy of its measurements in direct sunlight or other radiant heat sources. In worst cases when when the sensor is exposed to temperature conditions from -50 °C to 70 °C, the accuracy is ±0.60 °C. In conditions 0 to 70 °C the accuracy is ±0.10 °C [Campbell Scientific, 2022].

Figure 18: The 109 Temperature Probe (adapted from [Campbell Scientific, nd])

Temperature sensor with aluminum contact plate

Using the information and insights from the literature research, a temperature sensor prototype was designed and built within the diploma thesis work, incorporating an aluminum contact plate [Wuest, 2013]. The sensor comprised a polystyrene foam cube measuring 5 x 5 cm (Figure 19), an aluminum plate measuring 3 x 3 cm (Figure 24), and a Pt100 adhesive temperature sensor (Pt100, Omega engineering, Norwalk, USA). The temperature sensor was assembled by adhering a Pt100 temperature sensor to an aluminum plate (Figure 21) and then attaching it to a polystyrene cube (Figure 22).

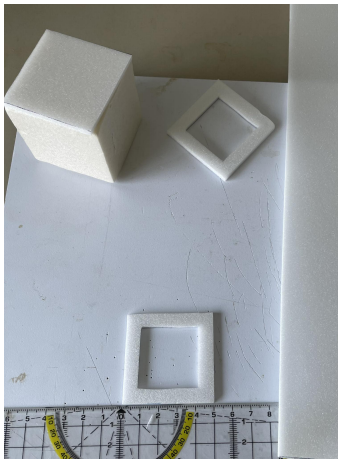

Figure 19: Polystyren cube

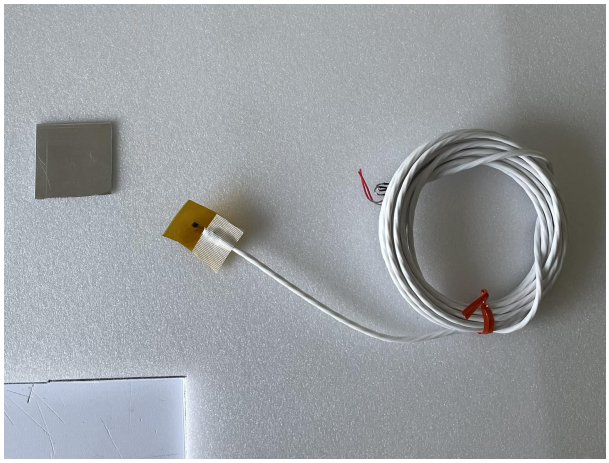

Figure 20: Alumunium plate and Pt100 adhesive temperature sensor

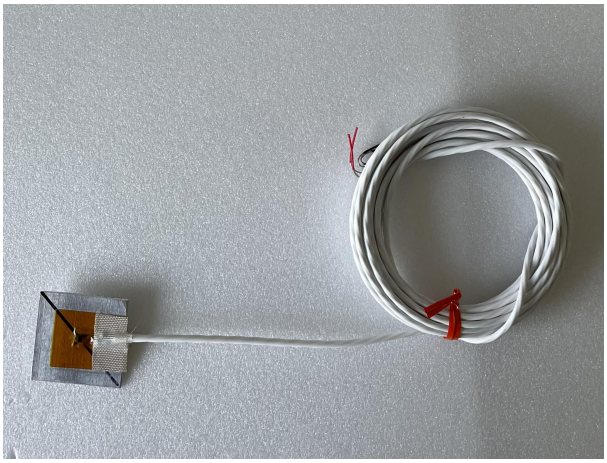

Figure 21: Pt100 temperature sensor glued to aluminum plate

Figure 22: Photograph of both temperature sensors used in the study

The measuring range of the Pt100 temperature sensor extends from -73°C to 260°C. The Pt100 temperature sensor is widely recognized for its exceptional precision and consistency, having an accuracy of ±0.06Ω at 0°C, in accordance with the DIN Class A standard. It has exceptional stability, with a drift of less than 0.2°C every year. The Pt100 has remarkable responsiveness, with 63% of its reaction occurring in under 0.9 seconds when covered in water, and a response time of less than 2 seconds on a heated surface. Furthermore, the sensor exhibits a self-heating effect of 2.5 milliwatts per degree Celsius (2.5 mW/°C), which emphasizes its efficient operational qualities [Jakar, 2023].

The polystyrene cube was chosen because of its low thermal conductivity and its act as an effective insulator. The selection of the aluminum plate was based on its exceptional thermal conductivity and relatively high specific heat capacity, enabling it to efficiently conduct and absorb substantial amounts of heat energy without experiencing a considerable increase in temperature [Jakar, 2023].

4.2 Laboratory work

Before the experiment, both temperature sensors underwent testing in a controlled laboratory setting. The aim of experiment was to determine the reaction time and accuracy of surface temperature measurements. The experiment was conducted on two distinct materials - LIAPOR, 4/8 (Lias Vintířov, Czech Republic) and ACRE, 19.4 (ACRE, s.r.o.; Czech Republic).

LIAPOR ceramic aggregate granulate is produced from plasticized Tertiary clays by firing in rotary kilns. The raw material for the production of ceramic aggregates is either harder shale or plastic clays. And Tertiary cypress clays from the overlying lignite seams of the Sokolov Basin are the raw material from which Liapor ceramic aggregate is produced. It contains minerals such as illite, kaolinite or silica, fragments of mica and also fossil remains [Liapor, 2024].

ACRE is a commercially available, green roof substrate, ahomogenised mixture of crushed spongilite (fraction 0-16 mm), crushed expanded clay and peat. It is suitable for undemanding plants such as mosses, sedges and some other dry-loving perennials and grasses that can do without watering in the long term [ACRE, 2021].

The temperature sensors underwent testing that involved measuring surface temperature of substrates. Substrate samples were placed in a tray and fully saturated with water. Subsequently, they were transferred to a freezer and kept there until the water solidified into ice. When melting occurs at the surface, the temperature of the substrate can be assumed to be 0°C. Subsequently, another experiment was conducted using a substrate heated to a higher temperature. Before taking this measurement, the substrates were subjected to a minimum of 24 hours of heating in an oven at a temperature of 50°C. The substrates were outfitted with temperature sensors that were weighted with objects to ensure full contact between the sensors and the surface. The response time and measurement rate of both sensors were evaluated.

Figure 23: Thin stainless steel probe on the iced substrate

Figure 24: Temperature sensor with aluminium plate and thin stainless steel probe on the iced substrate

4.3 Experiment on green roof

Location of the experiment

The experimental extensive green roof, where the temperature analysis carried place, is located on the premises of the University Centre for Energy Efficient Buildings (UCEEB), of Czech Technical University, on the north-western outskirts of the town of Buštěhrad in Central Bohemia region in Czech Republic (50°09'25.0"N 14°10'12.1"E) [Sněhota et al., nd] (Figure 25 - 27).

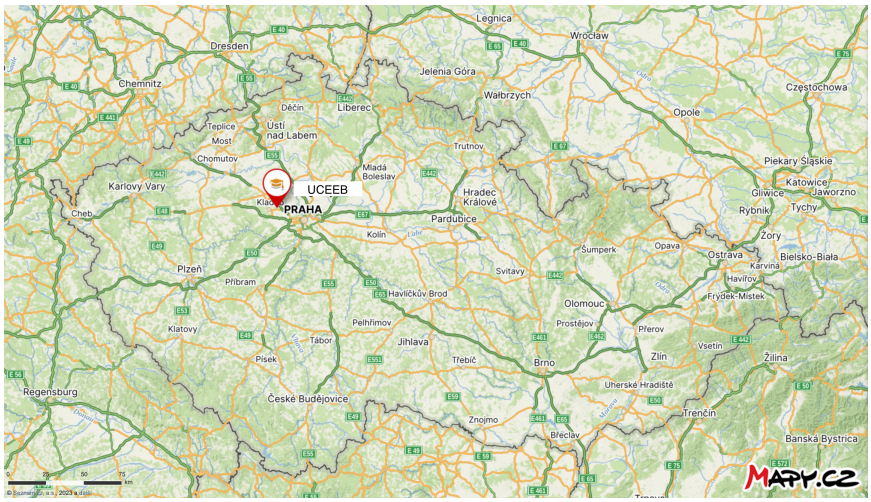

Figure 25: Map of the Czech Republic showing the location of UCEEB (edited from [Mapy.cz, 2024])

Figure 26: UCEEB with marked location of the experiment (edited from [Mapy.cz, 2024])

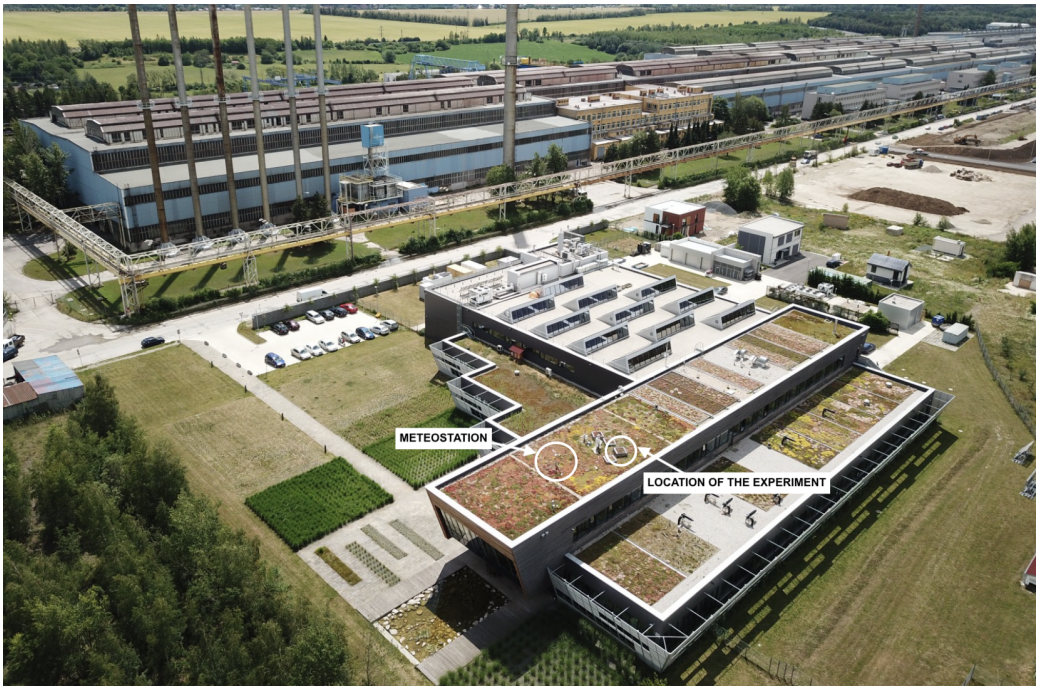

Figure 27: Location of the experiment (edited from [zel, 2023])

At three automated stations, UCEEB provides comprehensive monitoring of the hydrometeorological conditions surrounding the building. Three stations, consisting of two ground stations and one rooftop station, collect data on rainfall, soil and air temperatures, relative humidity, atmospheric pressure, wind speed and direction, and sun radiation. The rain gauges are positioned with their upper edges elevated 1.0 m above the surface they are measuring. Measurements of radiation, air temperature, relative humidity, wind speed, and wind direction are taken at an elevation of roughly 2 meters. The measurement of ground air temperature is conducted at a vertical distance of 5 cm from the surface. The rooftop weather station is situated on the expansive green roof of the UCEEB building, positioned at the greatest elevation of 365.3 meters above sea level. This station is the most well-equipped and extensively monitored [Sněhota et al., 2021]. The measurements conducted at this weather station provide valuable assistance for research operations related to water and energy dynamics in green roofs, among other topics. The local power grid supplies the data recorders at each fixed weather station with the necessary power, enabling them to make high frequency measurements. Simultaneously, all data loggers are equipped with battery backup power that allows them to operate for several hours to several hundred hours. This ensures that any power interruptions at the site will not result in data loss. Data is collected at regular one-minute intervals using CR1000 and CR3000 data recorders manufactured by Cambell Scientific, based in Logan, USA.

Experimental set up

In the experiment, sensors were installed on the green roof to observe the surface temperature of the experimental platform starting from August 2023 (Figure 29). The green roof being tested utilizes an ACRE EXTENSIVE substrate and is overlaid with a SEDUM TOP rhizome carpet. The layers of the test green roof are shown in the Figure 28. The plot consists of areas covered with plants, alongside with bare soil areas. The experimental area is equipped with measuring instruments that have been utilized to measure various factors such as air temperature, temperature beneath the green roof surface, precipitation, relative humidity, solar radiation, wind speed and direction, and rainfall.

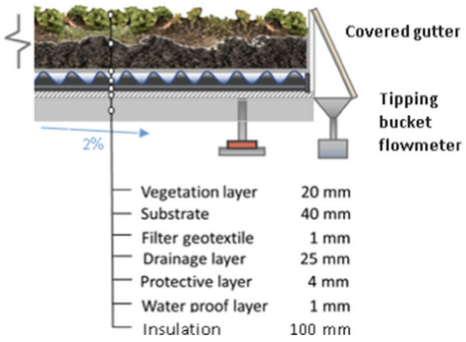

Figure 28: Scheme of the green roof test bed (adapted from [Sněhota et al., 2021])

Figure 29: Experimental green roof area

4.4 Temperature sensors installation

The experiment was set up on the morning of August 1, 2023. Three Thin stainless steel probes were placed on the bare soil of the green roof experimental area (as shown in the Figure 30). Additionally, another three identical temperature sensors were installed on the vegetated surface (as shown in the Figure 31). The temperature sensors were run horizontally at the same level as the surface of soil and were attached to the test surface using wires (Figure 32).

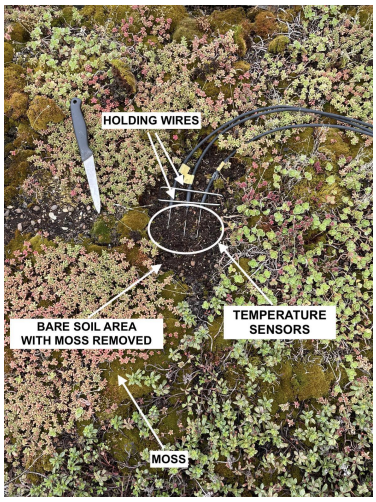

Figure 30: Installed sensors on bare soil

Figure 31: Photograph of sensors installed on the vegetated surface

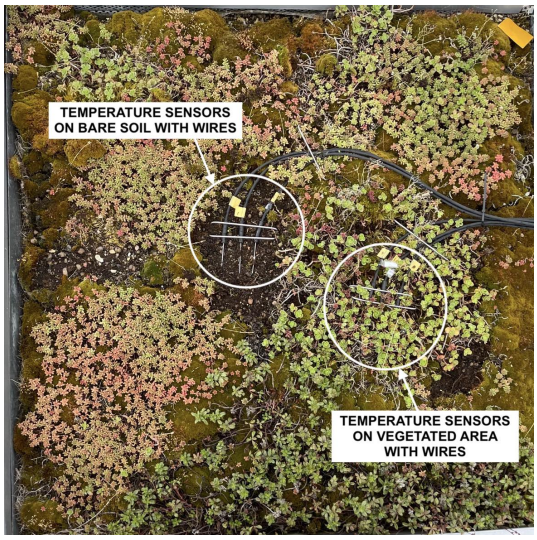

Figure 32: Location of temperature sensors on the test green roof

4.5 Measured data pre-processing and analysis

Various methods of evaluation were employed for visualizing the outcomes of the experiment. This subsection provides a comprehensive explanation and precise instructions on how to traverse the results accurately.

Box plots

The temperature and radiation data were plotted using box plots.

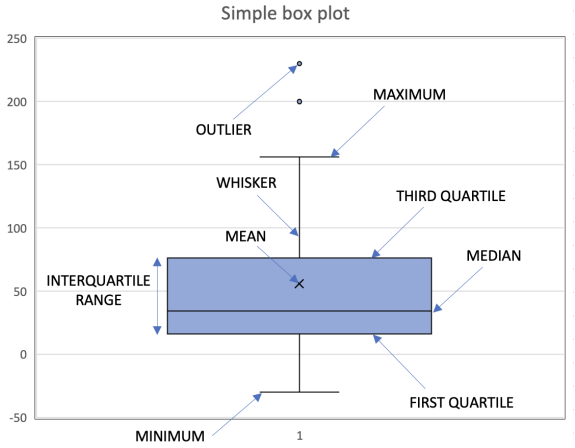

Figure 33: Simple box plot with

The median represents the central value of a dataset that has been arranged in ascending or descending order. This implies that precisely half of the elements are below the median, while the remaining a half are above the median.
The first quartile value (lower quartile) represents the data point that divides the sorted data set into four equal parts, with one quarter of the data falling below it. Exactly 25% of the items are below the first quartile, while exactly 75% of the elements are above it.
The third quartile value (upper quartile) represents the numerical point that divides the sorted data set into three equal parts, with three quarters of the data falling below this value. Exactly 75% of the items are below the third quartile, while 25% are beyond it.
The interquartile range (IQR) is the numerical value that represents the difference between the 1st quartile and the 3rd quartile. An observation is classified as an outlier if it surpasses a distance of 1.5 times the interquartile range below the first quartile or 1.5 times the IQR above the third quartile. Consequently, the upper whisker reaches the highest value in this range.

Model of surface temperature on bare soil

Experimental results were interpreted using a simple thermal model [Hong and Utzinger, 2021] that utilizes many actual data points and computes them using a formula with predetermined constant variables. The model requires knowledge of below surface substrate temperature. The formula used for this constructed model (which is a continuation of the chapter 3.3 Model of behaviour of temperature on bare soil):

$$T_{\text{surf,soil}} = \frac{I_{\text{solar}}\alpha_{\text{solar}} + 4\varepsilon_{\text{soil,surf}}\sigma(T)^3 T_{\text{sky}} + h_c T_{\text{air}} + \frac{k_e}{d} T_{\text{soil}} - \lambda E}{h_c + 4\varepsilon_{\text{soil,surf}}\sigma(T)^3 + \frac{k_e}{d}} \quad [10]$$

where:

$T_{\text{surf,soil}}$ ..... Temperature on the bare soil surface (K)
T_{sky} ..... Effective sky temperature (K)
T_{air} ..... Dry bulb temperature (K)
α_{solar} ..... Solar absorptance (%)
$\varepsilon_{\text{soil}}$ ..... Surface emissivity (%)
d ..... Soil depth at soil temperature measurement (m)
E ..... Evaporation rate (kg/m^{2}s)
I_{solar} ..... Avg. solar radiation within the time step (W/m^2)
k_{e} ..... Effective conductivity (W/mK)
h_{c} ..... Convection coefficient (W/m^{2}K)
σ ..... Stefan-Boltzmann constant (5,67.10^{-}8 W/m^{2}K^4)
λ ..... Latent heat of vaporization (approx. 2,43.10^6 J/kg)

Where h_{c} was determined from empirical equation:

$$h_c = 2.8 + 3V \quad [11]$$

where V is the velocity of the wind (m/s).

Variable T was determined from equation:

$$T = (T_{\text{air}} + T_{\text{sky}})/2 \quad [12]$$

$$E = \rho_{\text{air}} C V \frac{0.622}{P} 0.61078 \left(\exp\left(\frac{17.27 T_{\text{soil}}}{T_{\text{soil}} + 237.3} \right) - \exp\left(\frac{17.27 T_{\text{air}}}{T_{\text{air}} + 237.2} \right) \right) \quad [13]$$

where C is Dalton number and P is the total atmospheric pressure (Pa).

The model was computed using a MATLAB script (Appendix). The calculation was carried out without significant parameter optimization.

The provided input values consisted of solar radiation data (I_{solar}), wind speed (V), soil temperature (T_{soil}), and air temperature (I_{air}).

The variable values (Table 1) were chosen based on the information found in the literature.

VARIABLE	VALUE	UNIT
T_{sky}	270	K
α_{solar}	85	%
$\varepsilon_{\text{soil}}$	98	%
$\varepsilon_{\text{soil,sat}}$	99	%
$\varepsilon_{\text{soil,dry}}$	98	%
d	0,03	m
ρ_{air}	1,293	kg/m^3
k_{e}	0,432	W/mK
c	1,5.10^{-3}	m
P	101 325	Pa
h_{c}	10	W/m^{2}K
σ	5,67.10^{-8}	W/m^{2}K^4
λ	2,43.10^6	J/kg

Table 1: Estimated variables

From one study [Sadler, 1984] it was found that the average sky temperature is ranged from 245 - 275 K. So for our model the value of 270 K were selected for T_{sky}.

The solar absorptance, which varies between 0 and 1, is determined by the color of the surface [Perez, 2019]. In this scenario, the surface is bare soil with a dark brown colour. Therefore, a value of 0.85 was used for α_{solar}.

The surface emissivity ratings for bare soil range from 0.9 to 0.98 in dry conditions [Ni An, 2017].

A value of 0.98 was chosen for the dry surface emissivity, while a value of 0.99 was chosen for the saturated state.

Soil depth at soil temperature measurement is 0,03 m [Sněhota et al., 2021].

Air density is 1,293 kg/m^3 [NASA Earthdata, 2023].

The substrate's effective conductivity k_{e} was determined to be 0.432 W/mK in a previous study.

The standard atmosphere P is a unit of pressure defined as 101 325 Pa [Wikipedia, 2024].

Convection coefficient is 10 W/m^{2}K computed from equation [11].

Stefan-Boltzmann constant σ is 5,67.10^{-8} W/m^{2}K^4 [Young et al., 2014].

And latent heat of vaporization is 2,43.10^6 J/kg [Hong and Utzinger, 2021].

5 Results

This chapter presents the results derived from the thorough evaluations conducted on the collected data. Additionally, the outcome of performing a basic model is also displayed.

5.1 Laboratory work

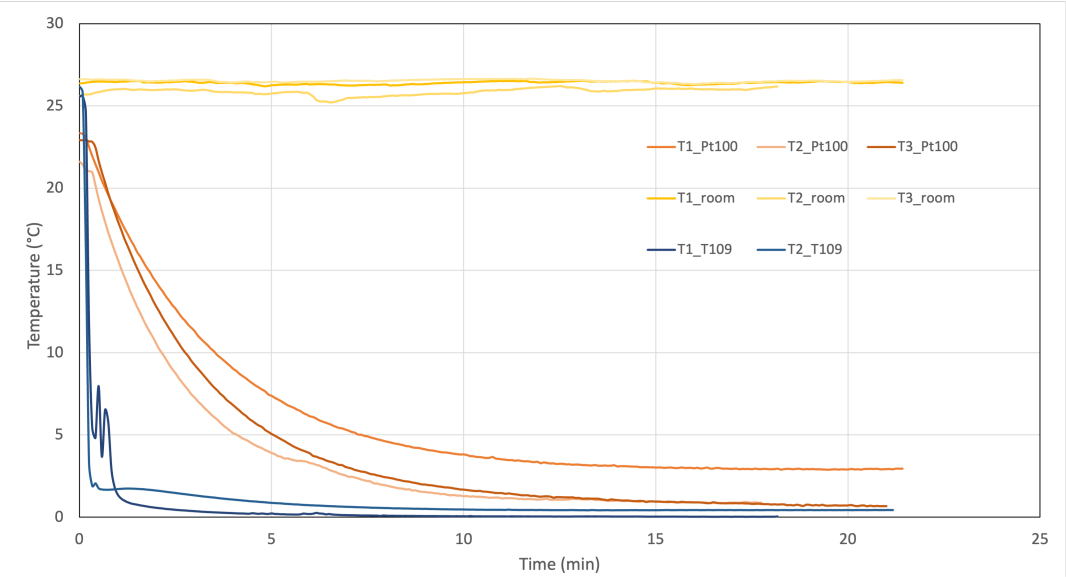

Figure 34: Graph of settling temperature sensors on frozen substrate

The Figure 34 shows the outcomes of a laboratory experiment conducted on soil that has been subjected to freezing conditions. The graph illustrates that the air temperature in the laboratory, as detected by the T109 temperature probe (T1_room, T2_room, T3_room), remained approximately at 26 °C during the duration of the experiment. During the settling period, the T109 temperature probe (T1_T109, T2_T109) attained a temperature close to 0°C, whereas the temperature sensor with aluminum contact plate (T1_Pt100, T2_Pt100, T3_Pt100) recorded a temperature that was 2-3°C higher. Furthermore, the thin stainless steel probe has a significantly quicker response time compared to the other one which indicates a steeper slope of the temperature curve at the beginning of the experiment.

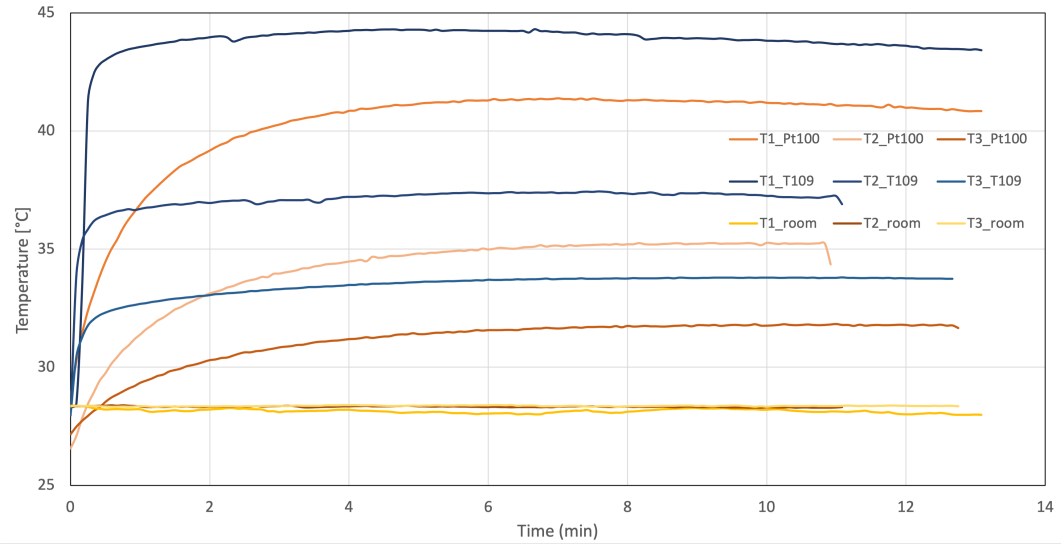

Figure 35: Graph of settling temperature sensors on heated substrate

The Figure 35 describes the outcomes of a study conducted on soil that was subjected to heat. The graph illustrates that the thin stainless steel probe (T1_room, T2_room, T3_room) recorded an average room temperature of approximately 28 °C throughout the experiment. During the settling period, the thin stainless steel probe (T1_T109, T2_T109, T3_T109) consistently recorded a temperature that was 2-3°C higher than the temperature sensor with aluminum contact plate (T1_Pt100, T2_Pt100, T3_Pt100). During the initial phase, the rapid ascent of the temperature curves for the thin stainless steel probe indicates a swift reaction to the applied heat, contrasting with the more gradual rise of the temperature sensor with aluminum contact plate.

5.2 Measurement on the experimental green roof

The experiment lasted from 2 August to 31 October, coinciding with the conclusion of the hydrologic year. Data were recorded in one-minute time steps for a duration of 13 weeks. Table 2 is a concise overview of the weeks.

WEEK	DATE
WEEK 1	02.08. - 08.08.
WEEK 2	09.08. - 15.08
WEEK 3	16.08. - 22.08.
WEEK 4	23.08. - 29.08.
WEEK 5	30.08. - 05.09.
WEEK 6	06.09. - 12.09.
WEEK 7	13.09. - 19.09.
WEEK 8	20.09. - 26.09.
WEEK 9	27.09. - 03.10.
WEEK 10	04.10. - 10.10.
WEEK 11	11.10. - 17.10.
WEEK 12	18.10. - 24.10.
WEEK 13	25.10. - 31.10.

Table 2: Overview of individual weeks of the study

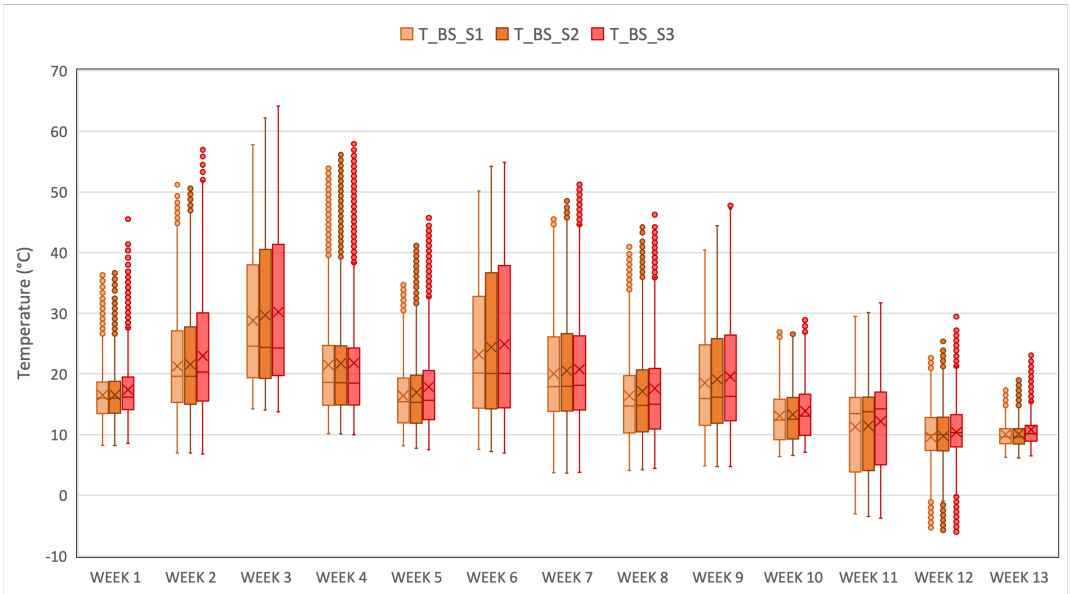

Figure 36: Box plot of temperatures measured on the part of experimental green roof with bare soil

The Figure 36 is a box plot illustrating the recorded temperatures on the exposed surface (bare soil) of the experimental green roof. This phenomenon is characterized by the consistent occurrence of higher temperatures being displayed by the third sensor compared to the other sensors, whereas the first sensor consistently displays the lowest temperatures. The peak temperatures occurred during the third week of August (WEEK 3), with the upper quartile values reaching approximately 40 °C, while the maximum values reached up to 64 °C. The minimum temperatures occurred during the WEEK 11, specifically in the second week of October, with a lower quartile of approximately 5 °C and the lowest extreme values dropping to -4 °C. In WEEK 12, the lowest temperatures are observed, reaching approximately -6 °C. The largest disparity between the upper quartile and the outlier points occurs during WEEK 4, with a temperature difference of around 30 °C. The greatest temperature variation occurs during the WEEK 6, namely in the 2nd week of September. Conversely, the smallest temperature variation is observed during WEEK 13, specifically in the last week of October.

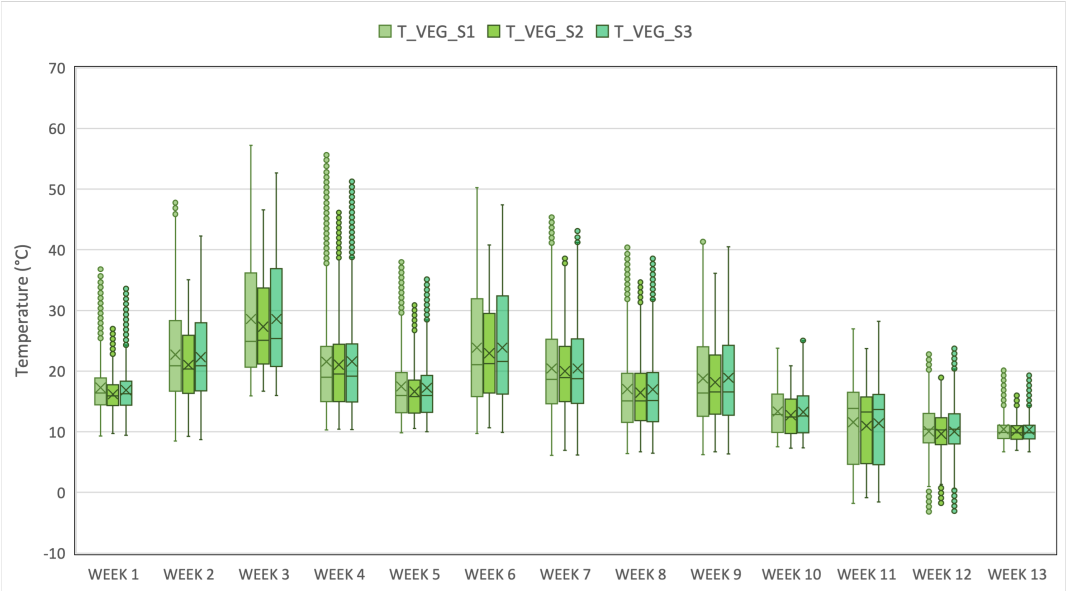

Figure 37: Box plot of temperatures measured on the part of experimental green roof with vegetation

The Figure 37 depicts the temperature readings obtained from sensors placed in vegetated areas on the green roof. It is feasible to compute almost perfectly recurring phenomena, wherein the second sensor consistently registers a temperature lower than the other sensors, with a variance of 0-4 °C. The peak temperature occurred during the third week of August, with upper quartile of temperatures ranging from relatively high to as high as 37 °C, while the maximum recorded value reached 57 °C. Conversely, the minimum temperature occurs during the WEEK 11, specifically the second week of October, with temperatures dropping to approximately 5 °C. Nevertheless, the isolated locations during the WEEK 12 exhibit considerably colder temperatures, approximately -3°C. The greatest disparity occurs during WEEK 4, where the upper quartile and the highest outlier can diverge by as much as 30 °C. The greatest temperature fluctuation occurs during WEEK 6, which corresponds to the second week of September, while the smallest fluctuation is observed in WEEK 13, which corresponds to the final week of October.

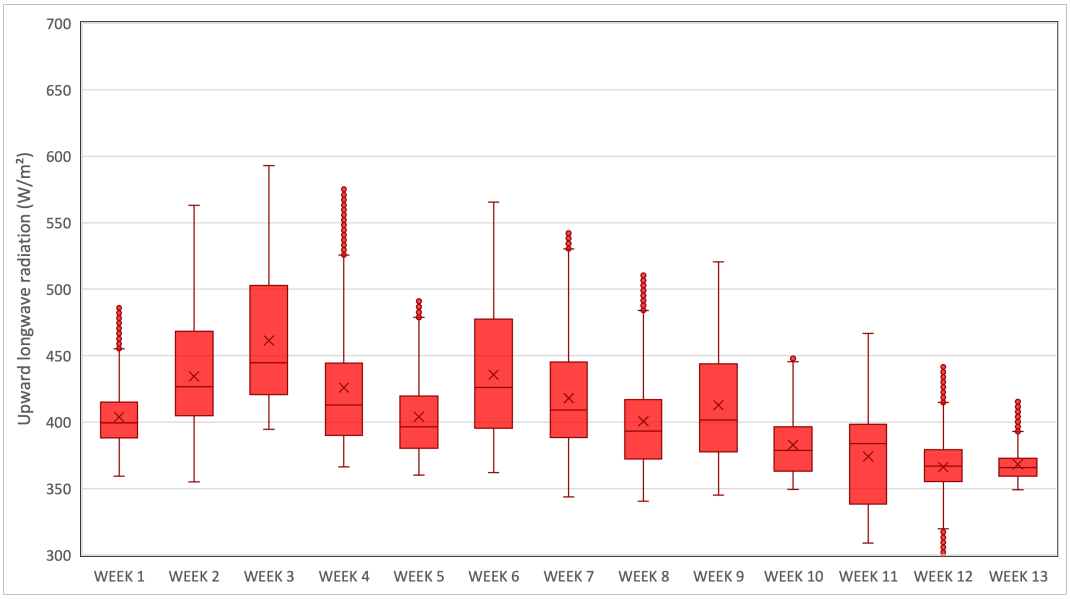

Figure 38: Box plot of upward longwave radiation

The Figure 38 is a box plot for upward longwave radiation on a green roof. The highest level of radiation is identified as an outlier in WEEK 3, representing the most extreme result in the entire dataset. It surpasses the upper quartile threshold of 500 W/m^2 and reaches a peak of over 600 W/m^2. The minimum radiation value is seen in WEEK 12, as indicated by the lowest whisker at around 300 W/m^2. WEEK 6 is notable for having the greatest median radiation, suggesting that it had the most significant average radiation levels compared to all other weeks. While WEEK 3 had the highest individual value, WEEK 6 displayed a greater range of data, as evidenced by the bigger interquartile range and multiple outliers. This suggests that WEEK 6 experienced a period of considerable variability in radiation. From WEEK 11 onwards, there is a noticeable tendency towards stability, with less variation and a decrease in radiation levels.

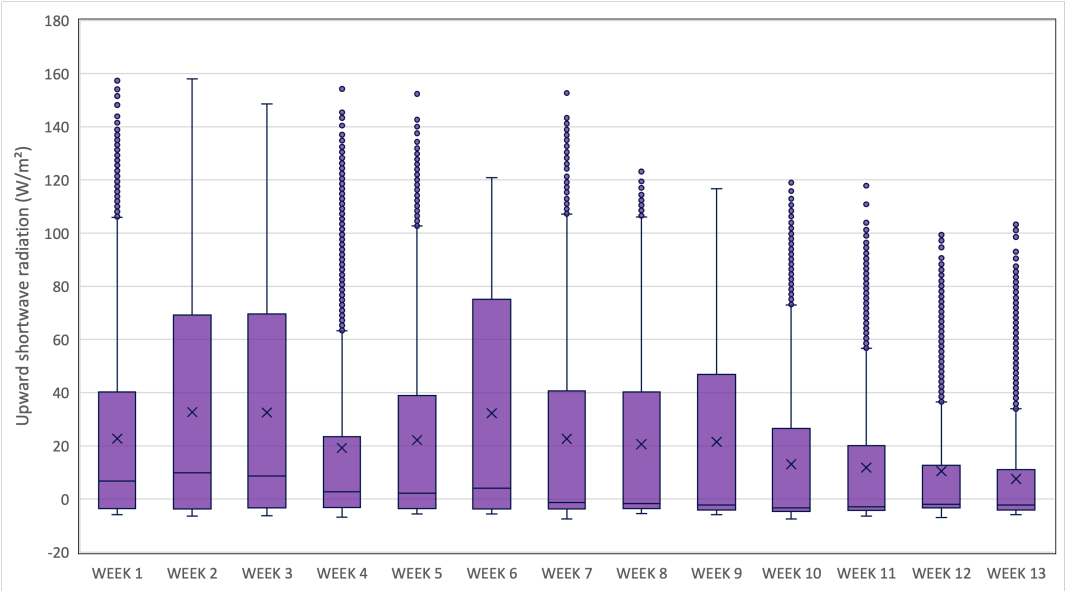

Figure 39: Box plot of upward shortwave radiation

The provided Figure 39 displays a box plot representing the values of upward shortwave radiation. WEEK 1 and WEEK 2 exhibit the highest median radiation levels, which denotes the mean, at a greater value relative to subsequent weeks. The upper whiskers of these weeks stretch to approximately 160 W/m^2, pointing to the presence of higher radiation values within the dataset. The box plots display a general decrease in the median radiation levels from WEEK 3 onwards, with WEEK 7 standing out due to an outlier that suggests an occasional dip towards 0 W/m^2, significantly lower than the typical range. WEEK 6 is distinguished by a high upper quartile, reaching 76 W/m^2, and a median around 10 W/m^2, reflecting a week with a generally higher radiation range compared to the median levels. The spread of the data, as shown by the interquartile range, varies week to week, illustrating the fluctuations in radiation levels that can occur.

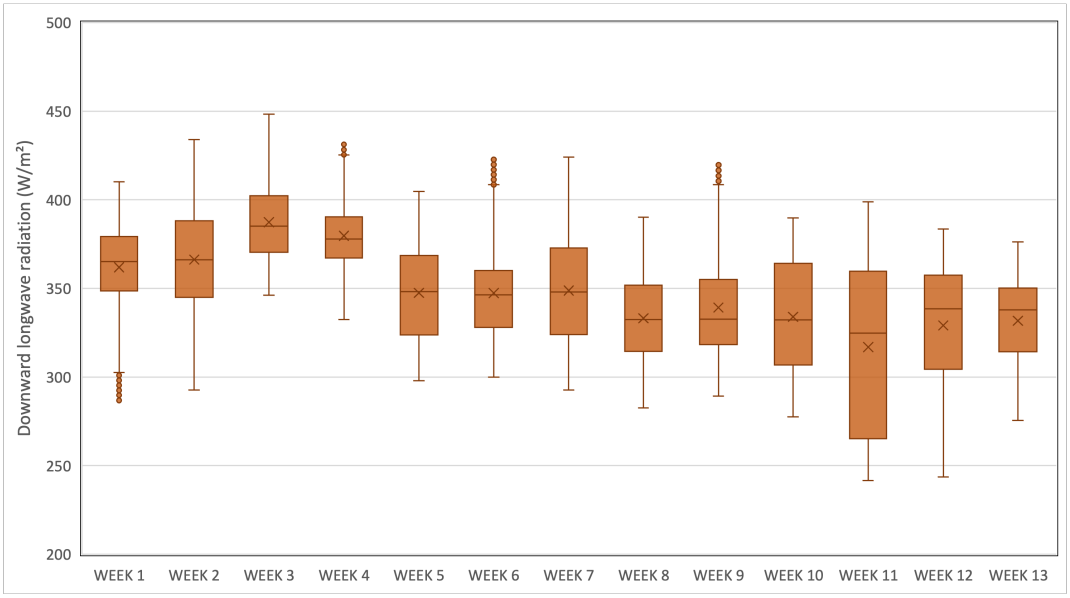

Figure 40: Box plot of downward longwave radiation

The box plot (Figure 40) of downward longwave radiation reveals that the peak value in the dataset is recorded in WEEK 3, indicating the largest emission of radiation during that week, with a value close to 450 W/m^2. Conversely, WEEK 11 is characterized by a considerable spread of data, with the box plot extending from an outlier at approximately 230 W/m^2, the lowest in the dataset, to higher quartile values. Week 3 has both the highest individual value and the highest median of 80 W/m^2, indicating that it regularly had higher average radiation emissions. WEEK 11 is notable for having the highest range of radiation levels, with data spanning from the lowest extreme to the higher quartile.

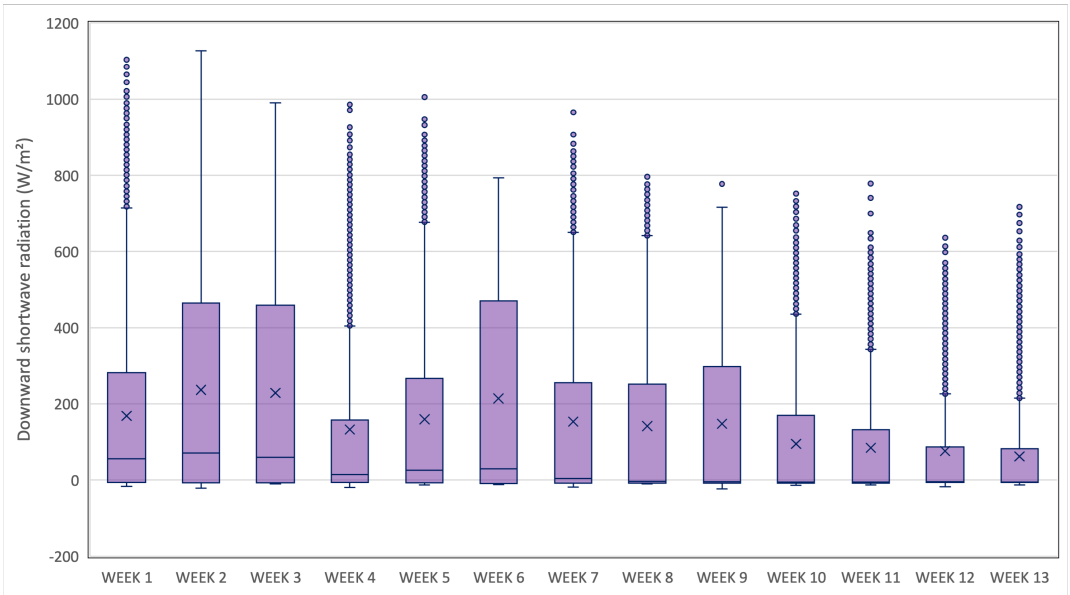

Figure 41: Box plot of downward shortwave radiation

The Figure 41 demonstrates the downward shortwave radiation, with the highest reflection value of 1120 W/m^2 of solar energy from the green roof occurring in WEEK 2. This week has the highest median value of 80 W/m^2, indicating a consistently elevated average amount of reflected solar radiation in comparison to other weeks. WEEK 6 exhibits the most extensive range of values, indicating a significant disparity between the lowest and highest reported radiation levels. The data from different weeks exhibit variety, with certain weeks, such as WEEK 2, having significantly higher medians. The minimum values seen each week are consistently comparable, hovering about 0 W/m^2.

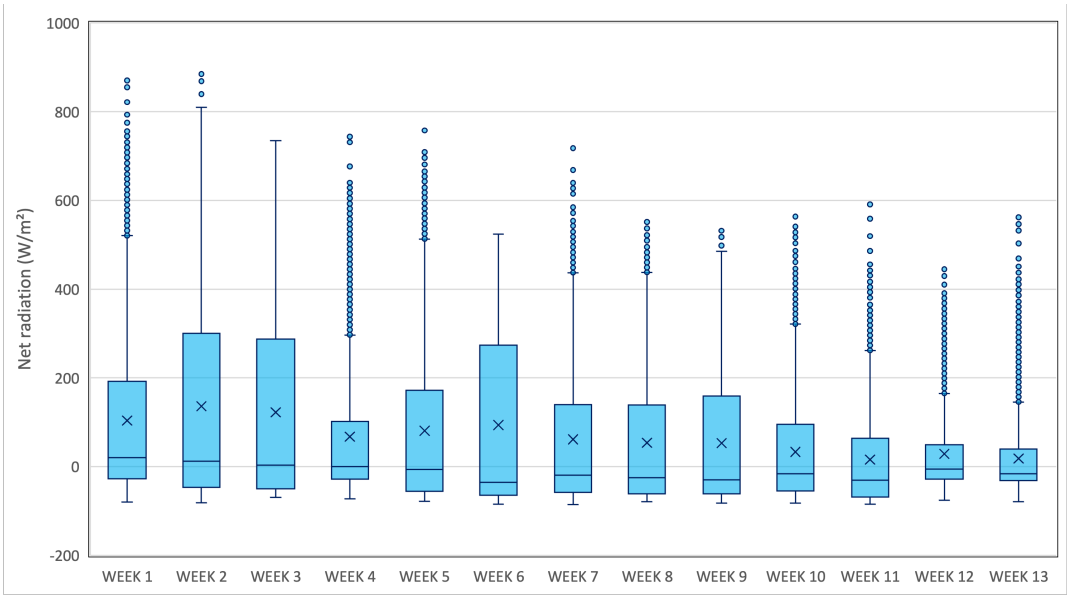

Figure 42: Box plot of net radiation

The Figure 42 illustrates box plot of the net radiation that was encountered on an extensive green roof of the UCEEB building within a 13-week time frame. WEEK 1 recorded the highest median value of net radiation at 20 W/m^2. In stark contrast, Week 6 is observed with the lowest median net radiation value of 35 W/m^2. WEEK 2 features a noteworthy outlier that peaks at 890 W/m^2, significantly higher than the median. This outlier corresponds with the highest mean value of 135 W/m^2 across all weeks underscoring the presence of intense radiation during that week. Conversely, WEEK 11 demonstrates the lowest average value of net radiation at 15 W/m^2. This week also shows a broad range of values, extending from the lowest recorded radiation to higher quartile values.

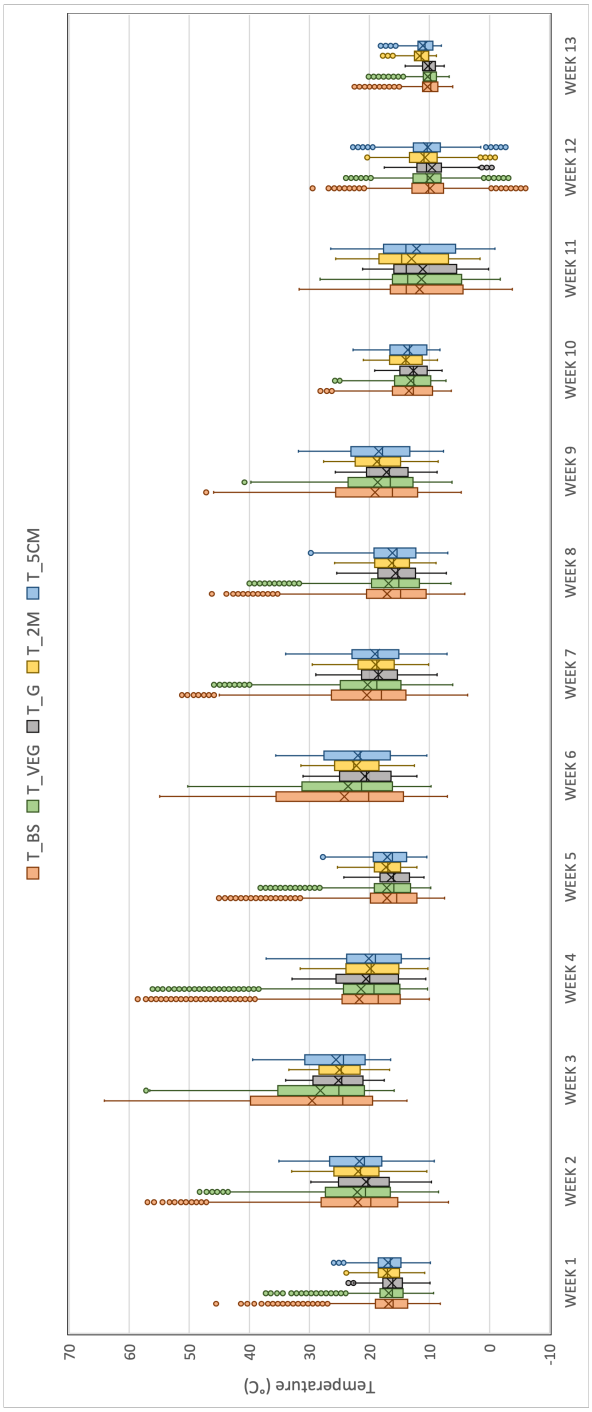

Figure 43: Temperatures of bare soil, area with vegetation, subsurface of substrate and temperatures in 2m and 5cm above the green roof

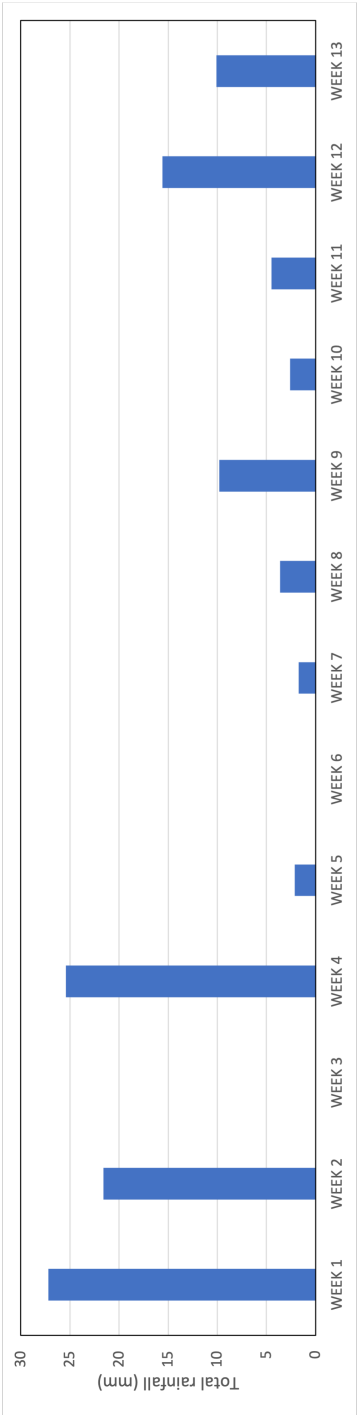

Figure 44: Total weekly rain amounts

The temperature dynamics of an experimental green roof, as depicted by the box plot (Figure 43), exhibit clear patterns across five unique measurement variables over a span of thirteen weeks. WEEK 3 had the greatest median temperatures across all variables, including bare soil (T_BS), vegetation (T_VEG), in-soil (T_G), 2 meters above the roof (T_2M), and 5 centimeters above the roof (T_5CM). WEEK 6 displays the most pronounced variation in temperatures, especially in the bare soil layer (40 °C), and also has the highest number of outliers, indicating a large temperature amplitude during this period. WEEK 13, in contrast, displays the lowest median temperatures across all variables. Both the surface temperature, ranging from 9 to 11 °C, and the subsurface temperature have nearly identical values for the first time. WEEK 12 experienced the most extreme outliers with temperatures dropping to -6°C, while WEEK 13 had the lowest median values. The conspicuous anomalies observed in WEEK 4, across several metrics, underscore this week as a period of extraordinary temperature fluctuation, the surface temperatures exhibit upper quartiles of approximately 24 °C, with outlying values reaching up to 58 °C for bare soil and 56 °C for the sensor in vegetation.. The sensors placed on bare soil consistently register greater temperatures than those placed within vegetation, indicating a repeating pattern. Furthermore, it is typically seen that the temperature recorded in the soil is consistently lower than the temperature recorded on the vegetated surface. Typically, the surface temperature is higher than the subsurface temperature. However, in WEEK 4, the subsurface temperature is higher, and its highest upper quartile is nearly 2 °C higher than the surface temperature. By the WEEK 13, both surface temperatures and subsurface temperatures exhibit a near-equivalence. During the first 10 weeks, the temperature at a height of 2 meters above the green roof consistently exceeds the temperature 5 cm above the surface of the green roof. However, starting from the eleventh week, the situation reverses.

The bar chart (Figure 44) depicts the cumulative weekly precipitation for a thirteen-week time frame, with a prominent spike in Week 1, signifying the maximum amount of rainfall recorded. Subsequently, there is a significant decline, with WEEK 3 and WEEK 6 recording the minimum precipitation, indicating a period of arid weather. WEEK 2 and WEEK 4 stand out due to their comparatively significant levels of precipitation, with WEEK 4 being the second highest in the sequence.

Comparison of measured temperatures on bare soil and area with vegetation with effect of air temperature

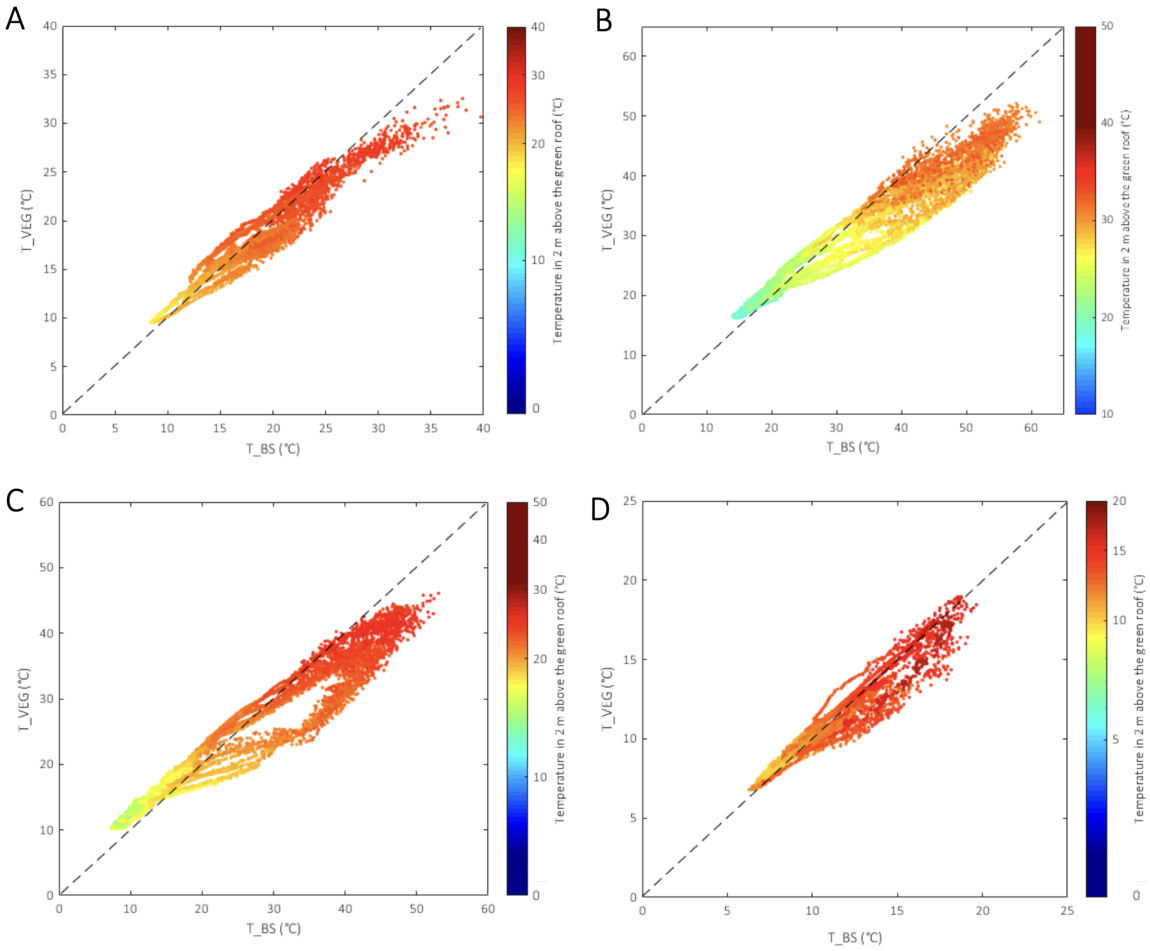

Figure 45: Relationship between the temperature of bare soil and part with the vegetation with air temperature in A) WEEK 1 B) WEEK 3 C) WEEK 6 D) WEEK 13

The scatter plots (Figure 45) illustrate a direct relationship between the temperatures of the bare soil (T_BS) and the vegetated parts (T_VEG) on a green roof. The color gradient represents the air temperature 2 meters above. In all four plots the majority of data points are positioned below the dashed diagonal line, suggesting that vegetated regions tend to have lower temperatures compared to bare soil. The dispersion of the data points indicates the presence of variability in this cooling phenomenon, which seems to be more prominent at mild soil temperatures and decreases as the soil temperature increases. When the soil temperatures rise, the cooling effect of vegetated regions decreases, causing the air temperature above the green roof to

increase dramatically. This is evident from the concentration of red points at the upper end of the color scale.

In WEEK 1 (A), the temperature of soil surface reaches values from 10°C to 40°C and the range of air temperature is from 18°C to 35°C. The range of soil surface temperatures in WEEK 3 (B) is 13°C to 60°C, whereas the range of air temperatures is 18°C to 40°C. The soil surface temperature in WEEK 6 (C) ranges from 8°C to 53°C, whereas the air temperature is between 13°C and 30°C. In WEEK 13 (D), the air temperature is between 8°C and 20°C, while the soil surface temperature varies from 6°C to 20°C.

Comparison of measured temperatures on bare soil and area with vegetation with effect of net radiation

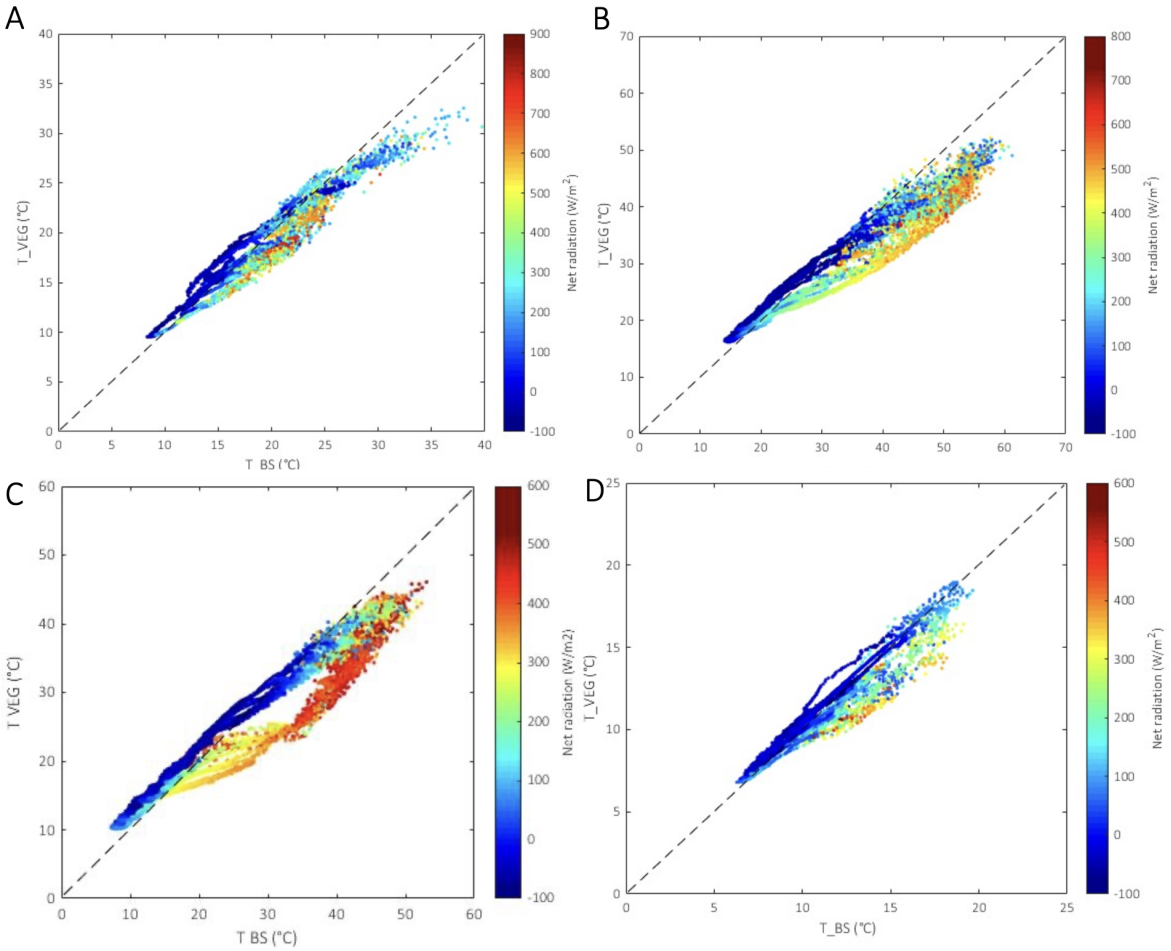

Figure 46: Relationship between temperature of bare soil and part with the vegetation with net radiation in A) WEEK 1 B) WEEK 3 C) WEEK 6 D) WEEK 13

The scatter plots (Figure 46) show the correlation between the temperature of the bare soil (T_BS) and the temperature of the vegetated sections (T_VEG) on a green roof. The color of each data point represents the amount of net radiation impacting the roof. The plot forms a tightly packed, diagonal cluster that extends from lower left to upper right, suggesting a strong, positive correlation between T_BS and T_VEG temperatures. The data points predominantly cluster below the diagonal dashed line, suggesting that vegetated regions generally exhibit lower temperatures compared to bare soil, regardless of the quantity of net radiation.

As for the effect of net radiation, indicated by the color gradient ranging from blue to red, the densest areas of blue (representing lower net radiation levels) are

situated at the lower end of the temperature scale. Consequently, lower temperatures are correlated with decreased net radiation. As temperatures rise, net radiation levels likewise increase, progressing from green to yellow, and ultimately to red at the greatest temperatures and radiation levels.

In WEEK 1 (A), the temperature of soil surface reaches values from 10°C to 40°C and the range of net radiation is from 0 to 750 W/m^2. The range of soil surface temperatures in WEEK 3 (B) is 13°C to 60°C, whereas the range of net radiation is 0 to 650 W/m^2. The soil surface temperature in WEEK 6 (C) ranges from 8°C to 53°C, whereas the net radiation is between 0 and 600 W/m^2. In WEEK 13 (D), the net radiation is between 0 and 450 W/m^2, while the soil surface temperature varies from 6°C to 20°C.

Comparison of measured temperatures on bare soil and area with vegetation with effect of Downward shorwtwave radiation

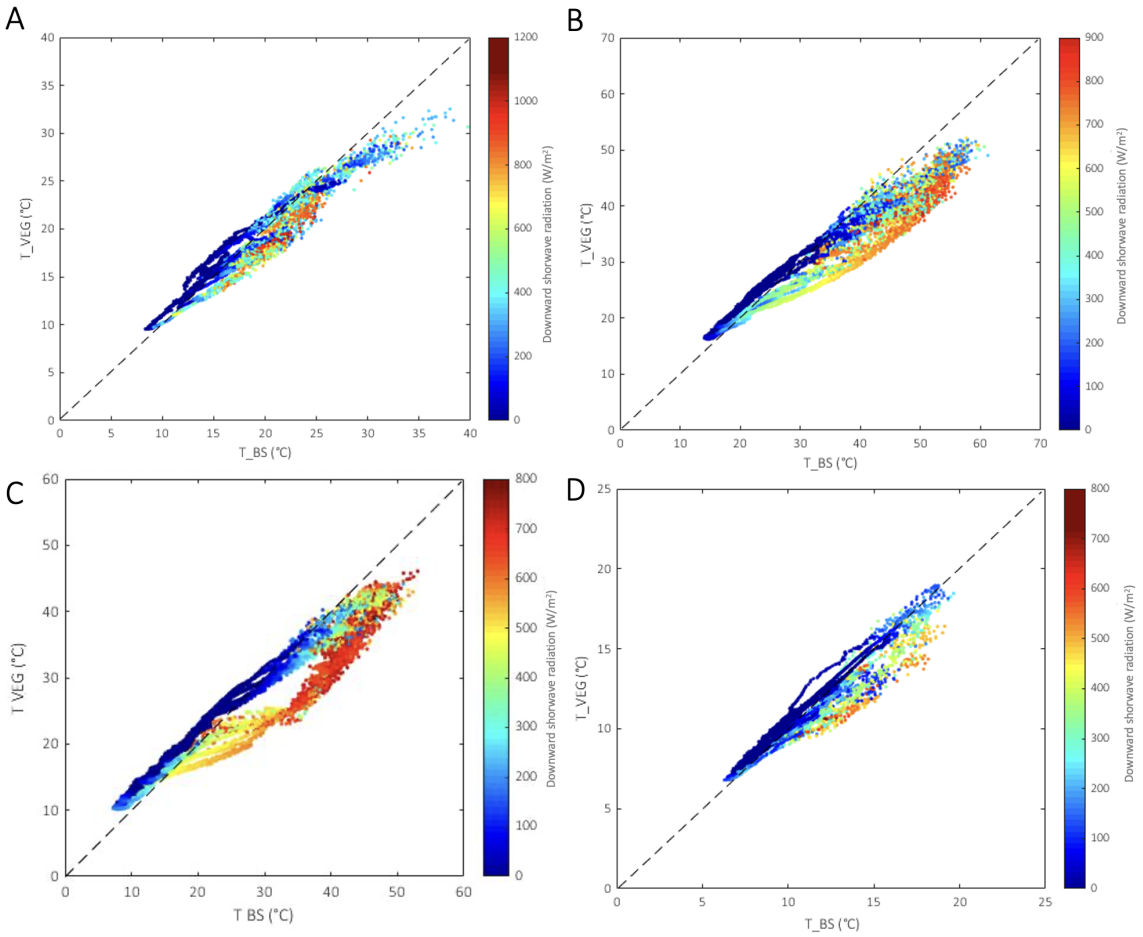

Figure 47: Relationship between temperature of bare soil and part with the vegetation with downward shortwave radiation in A) WEEK 1 B) WEEK 3 C) WEEK 6 D) WEEK 13

Figure 47 illustrates the correlation between the temperatures of exposed soil (T_BS) and vegetated regions (T_VEG) on a green roof. The color of each data point indicates the impact of downward shortwave radiation. The color gradient corresponds to the intensity of the upward shortwave radiation. It is observed that the lower end of the temperature range is predominantly blue, indicating lower radiation levels. With rising temperatures, the colors transition from green to yellow and finally to red, indicating elevated quantities of downward shortwave radiation.

The observed change in shade indicates a positive correlation between higher surface temperatures and increased downward shortwave radiation. The area with the greatest abundance of blue, and thus the least amount of radiation, is found in

regions where T_VEG is below T_BS. The graph illustrates a positive correlation between rising temperatures and an increase in downward shortwave radiation.

In WEEK 1 (A), the temperature of soil surface reaches values from 10°C to 40°C and the range of downward shortwave radiation is from 0 to 1 000 W/m^2. The range of soil surface temperatures in WEEK 3 (B) is 13°C to 60°C, whereas the range of downward shortwave radiation is 0 to 800 W/m^2. The soil surface temperature in WEEK 6 (C) ranges from 8°C to 53°C, whereas the downward shortwave radiation is between 0 and 800 W/m^2. In WEEK 13 (D), the downward shortwave radiation is between 0 and 550 W/m^2, while the soil surface temperature varies from 6°C to 20°C.

Comparison of measured temperatures on bare soil and area with vegetation effect of increasing and decreasing temperature

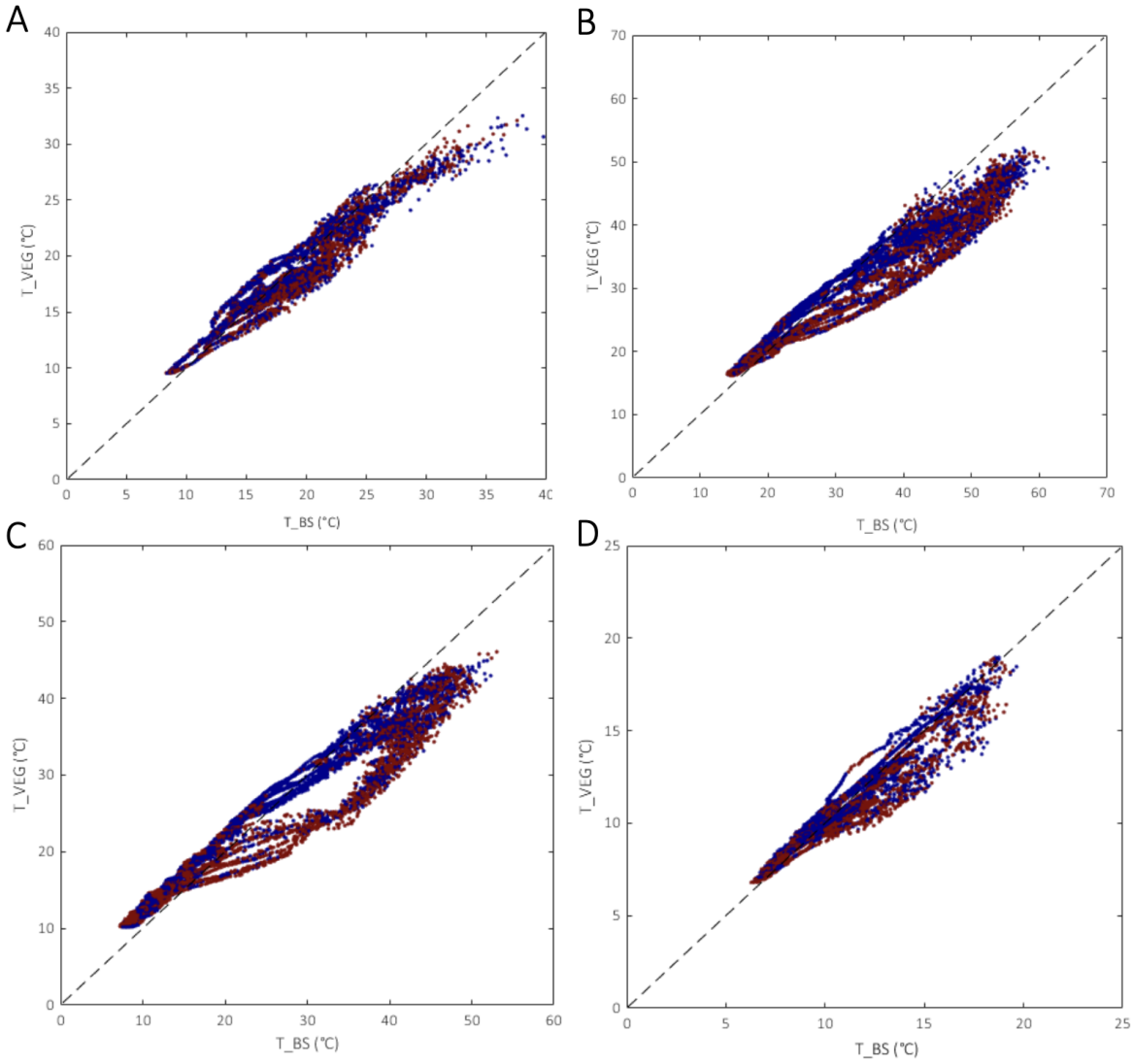

Figure 48: Relationship between temperature of bare soil and part with the vegetation with temperature change in A) WEEK 1 B) WEEK 3 C) WEEK 6 D) WEEK 13 with increasing color red and decreasing color blue

The scatter plots (Figure 48) depict the relation between the temperatures of the exposed soil (T_BS) and the vegetated regions (T_VEG) on a green roof, with the color of each data point indicating changes in air temperature. Red points represent times of increasing air temperature, while blue points indicate periods of decreasing air temperature. There is an apparent arrangement of data points forming a diagonal

cluster, running from the lower left to the upper right. This suggests that when the temperature of the bare soil increases, the temperature of the vegetated area also tends to ascend. The arrangement of red and blue points along this diagonal indicates that air temperature changes, including both rises and falls, are happening over the whole spectrum of observed soil and vegetation temperatures. The concentration of red points seems to be denser at higher temperatures, indicating that air temperature is more likely to increase when the surface temperatures are higher. In contrast, blue points are dispersed across the data, with a particular concentration near the lower end of the temperature range.

Simple model of surface temperature on bare soil

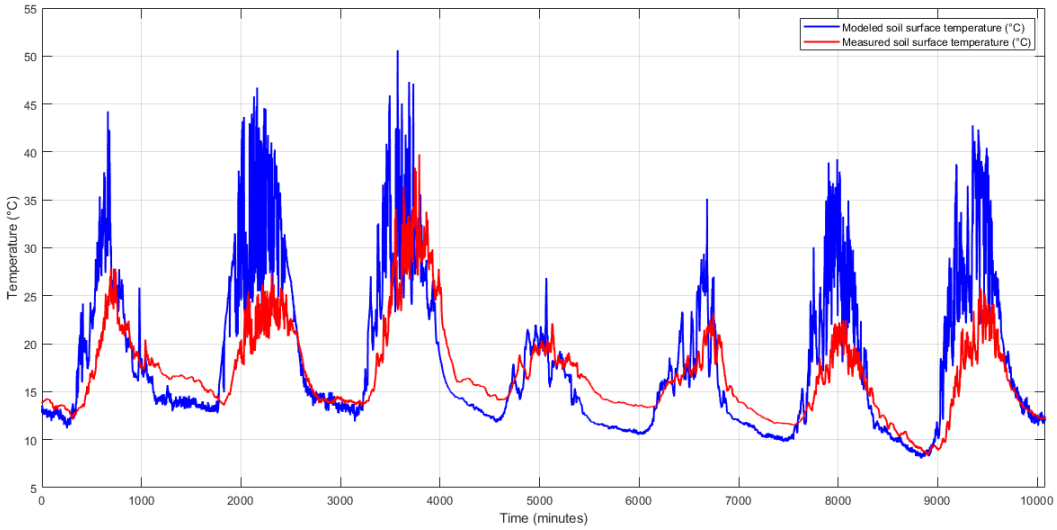

Figure 49: Comparison of measured and modeled soil surface temperature in WEEK 1 (highest rainfall)

The graph (Figure 49) presents a comparison of measured and modeled surface temperatures on a substrate, both in one minute interval, during a WEEK 1 characterized by the highest rainfall. The blue line represents the modelled soil surface temperature, whereas the red line represents the actual measured soil surface temperature. Both temperature profiles have a significant cyclic pattern that aligns with daily thermal cycles, reaching their highest point during daylight hours and decreasing during the night. The model's result in overall follows the measured temperatures, capturing the overarching trends and periodic temperature shifts. However, there are significant cases where the simulated temperatures deviate from the observed data. Specifically, during the peak daytime temperatures, the model often overestimates the intensity of the heat and it has almost 20 °C difference. Conversely, at night, the model occasionally underestimates the temperature in comparison to measured values.

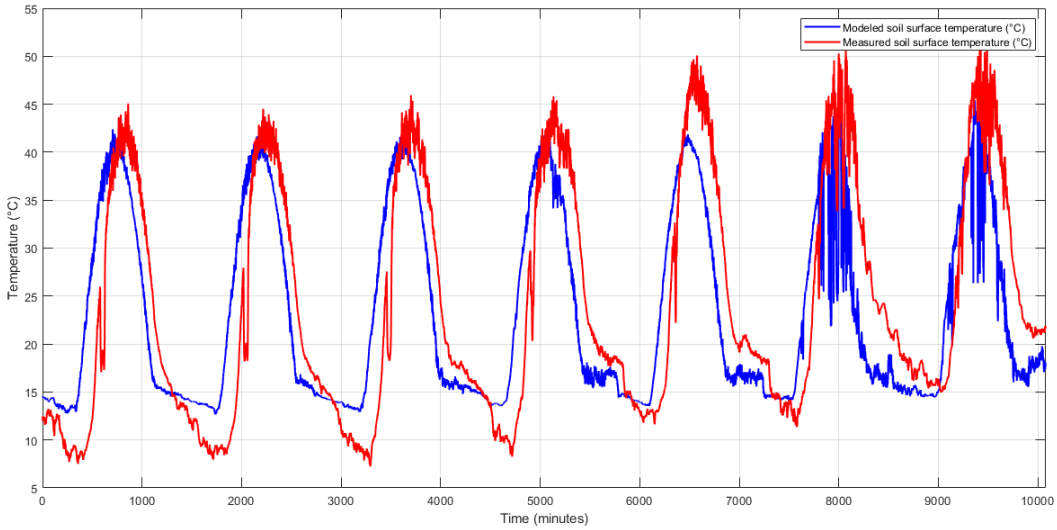

Figure 50: Comparison of measured and modeled soil surface temperature in WEEK 6 (no rainfall)

The graph (Figure 50) portrays the soil surface temperature profiles over WEEK 6, a period characterized by an absence of rainfall, with time plotted in minutes. The modelled soil surface temperature is again illustrated by the blue line, while the actual measured soil surface temperature is depicted in red. During this dry week, both temperature curves exhibit distinct diurnal patterns, with temperatures rising sharply during the day and falling steeply at night. The modelled data generally captures the shape of the temperature fluctuations, following the measured data's trend closely. However, there are moments when the model underestimates the daytime peak temperatures. Similarly, during nighttime, the model occasionally overestimates the cooling. The variation between the model and the measured data during this rainless week is not higher then 8 °C.

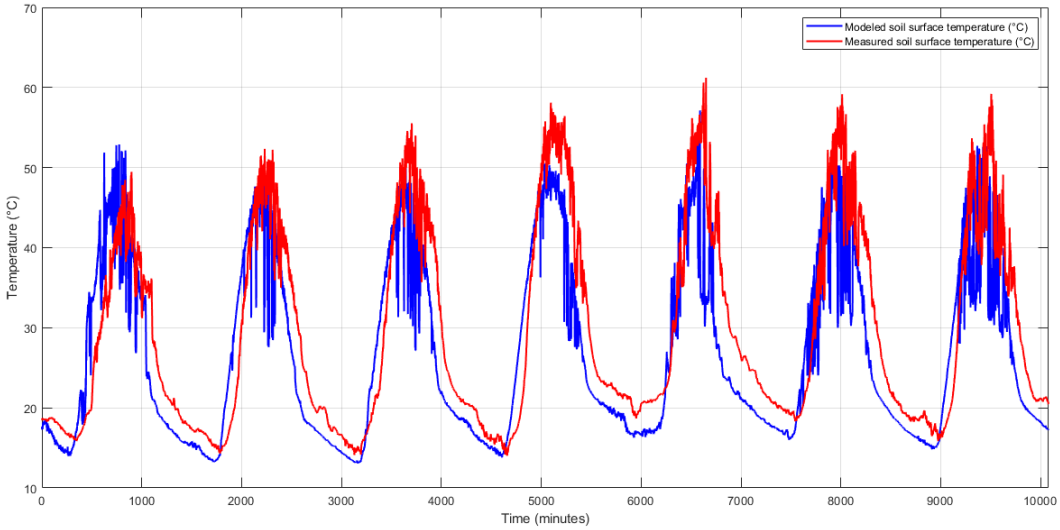

Figure 51: Comparison of measured and modeled soil surface temperature in WEEK 3 (highest temperature)

This graph (Figure 51) illustrates the fluctuation of soil surface temperature during WEEK 3, which noticed the maximum temperatures. The data was collected at minute intervals. The graph compares the simulated soil surface temperature, represented by the blue line, with the measured soil surface temperature, highlighted in red. Both datasets exhibit pronounced cyclical patterns that align with the diurnal temperature cycle, with sharp temperature spikes occurring during daylight hours and significant drops during the night, accentuated during this week by the extreme temperatures. The comparison reveals a clear trend of the modelled temperatures closely shadowing the measured values. However, there are distinct intervals in which the model inaccurately calculates the actual measured temperatures, namely during the noon and the cooling periods at night. During the highest points of the day, the model seems to evaluate the maximum temperatures lower than the actual ones. On the first day, the model exhibits a greater value, whereas on following days, the model's values are consistently lower than the actual values. The disparities between the model and actual values fluctuate between 3 and 10 °C during peak daylight hours, while at night the disparities are approximately 4 °C or lower. The biggest difference occurs on the fourth day, with a temperature difference of 10 °C between the highest points of both curves, and a 4 °C difference at night.

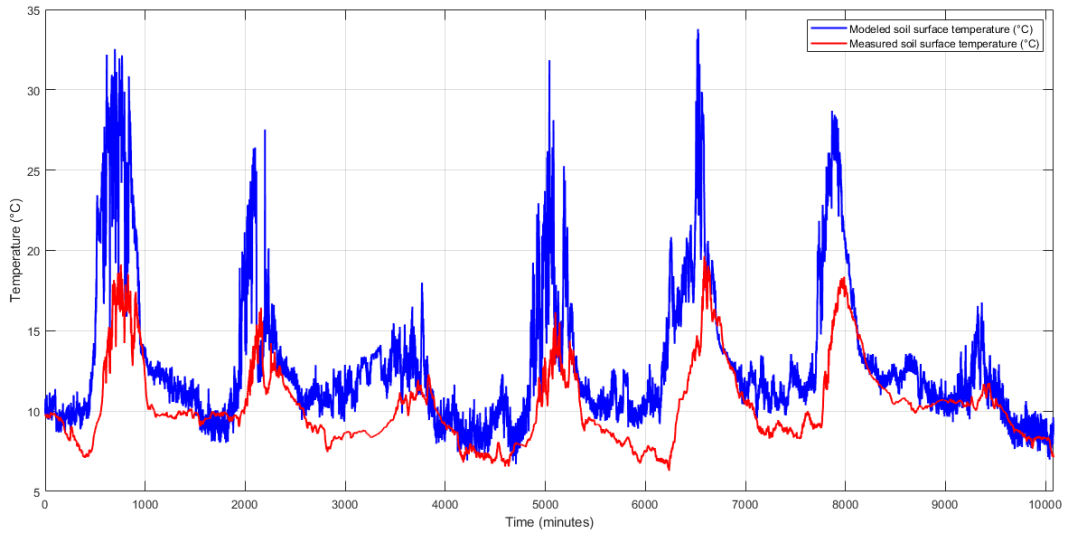

Figure 52: Comparison of measured and modeled soil surface temperature in WEEK 13 (lowest temperature)

The Figure 52 presents a direct comparison between the predicted and measured soil surface temperatures for WEEK 13, which is week with the lowest found temperatures. The blue line represents the modelled soil surface temperature, while the red line corresponds to the actual measured temperature. The peaks, corresponding to daytime highs, are low, and the nighttime lows dip further. Despite the reduced temperature range, the modelled data still tracks the general pattern of the measured temperatures. However, during the coldest peaks, the model tends to overestimate the actual soil surface temperature. Conversely, in some instances during the night, the model slightly overestimates the temperature. The model also seems to be less responsive to sudden temperature drops, which are typical during the coldest periods. The most significant deviations between the modelled and measured data occur during transitions between day and night. During peak daylight hours, the differences between the model and actual values vary between 10 and 15 °C, whereas at night, they are between 0 to 9 °C. On the fourth day, there is a significant disparity in temperature between the highest points of both curves, with a variation of 15 °C. Additionally, there is a 10 °C difference in temperature during the night.

6 Discussion

6.1 Laboratory experiments

The analysis of temperature sensor performance reveals that the thin stainless steel probe has a significantly faster reaction time to changes in temperature than the temperature sensor with an aluminum contact plate. The rapid reaction capabilities of the thin stainless steel probe is demonstrated by the steeper slope in the beginning of its temperature curve observed during the experiment.

The thin stainless steel probe exhibited exceptional detecting abilities in a setting with partly frozen materials by accurately recording temperatures near 0°C, suggesting its superior performance in cold settings. In addition, it quickly adapted to changes in temperature, demonstrating its adaptability in detecting both drops and increases in temperature quickly.

The temperature sensor with an aluminum contact plate exhibited significantly slower response time. The graph's smooth curves indicate more stabile behavior, which however can't be taken as a positive attribute, but rather as a result of a long reaction time.

It is important to acknowledge that the thin stainless steel probe regularly registered temperatures that were 2-3°C higher than those measured by the temperature sensor with contact aluminum plate. This disparity may suggest an increased sensitivity to changes in temperature or transferring the heat to the sensor from the surrounding environment.

While the aluminum plate is has excellent heat transfer capabilities [Ramos et al., 2012], contributing to the stability of the Pt100 sensor's readings in certain conditions, its effectiveness in a soil environment, particularly with frozen substrates, has not been fully proven. The combination of the Pt100 sensor and aluminum plate, though achieving consistent temperature distribution and potential accuracy in stable conditions, faces limitations. These include a slow reaction time and an inability to equilibrate with the real surface temperature of frozen substrates.

The thin stainless steel probe is ideal for scenarios that need quick identification of temperature fluctuations, but the temperature sensor with aluminum contact plate excels in providing reliable and steady monitoring at smooth, flat surfaces (ie steel slab), potentially yielding more precise measurements over a prolonged period of time. Due to our preference needs, the experiment was eventually conducted with a thin stainless steel probe only .

6.2 Measurement on the experimental green roof

Temperature on surface level of bare soil

The temperature data obtained from Figure 36 reveal various patterns and anomalies during the 13-week period on the bare soil of the experimental green roof. The third sensor consistently shows higher temperatures compared to the others, which may be attributed to its specific location on the surface, potentially receiving more direct sunlight or being less affected by wind cooling [Van Bavel and Hillel, 1976].

The first sensor's location might be in a shaded area or near a thermal mass like dense vegetation, known for absorbing heat, which could moderate temperature fluctuations. Additionally, the sensor's specific placement could result in increased exposure to wind, further enhancing convective cooling. This combination of factors, particularly the sensor's distinct contact with the green roof's surface, could explain why it consistently shows colder temperatures compared to the other sensors [Horton and Ochsner, 2011].

The highest temperatures recorded during the third week of August (WEEK 3) align with the peak of summer, where were higher solar radiation (Figure 42) and rainfall free conditions (Figure 44), leading to intensified heating of the roof surface indicating the relationship between temperature and radiation [Hillel, 2014]. The upper quartile values, which reached around 40°C during this period, may be explained by prolonged sun exposure and potentially low wind conditions that limit the cooling impact.

In contrast, the coldest temperatures experienced during the second week of October (WEEK 7) align with the shift into cooler fall weather. The decrease in temperature to around freezing, as shown by the lower quartile and extreme values, implies the beginning of colder evenings and the potential possibility of the first frosts, which are typical for this season [Van Bavel and Hillel, 1976].

The highest temperature fluctuation takes place in WEEK 6, specifically in the second week of September. This phenomenon may be attributed to a transitional phase between seasons, during which there is a tendency for day-to-night temperature fluctuations to be more noticeable.

In contrast, the minimal temperature fluctuation recorded in WEEK 13, which falls in the last week of October, indicates a more stable thermal conditions characterized by reduced solar radiation (Figure 42) and probably more uniform cloud coverage [Hillel, 2003].

Temperature on surface level of part with vegetation

The temperature data collected from the experimental green roof (Figure 37) presents a complex interplay of environmental factors influencing roof vegetation. Particularly, the variability in temperature readings across different sensors suggests microclimatic variations within the vegetated area despite the sensors are located in the nearest proximity [Hillel, 2003, Hillel, 2014]. For instance, the consistently lower readings from the second sensor may indicate a localized shade effect or a higher water retention capacity in that area, both of which could result in cooler temperatures. Also the level of contact with the surface of soil may have a significant influence.

The highest temperatures seen during the third week of August (WEEK 3) align with the typical weather patterns for the area, when the summer heat reaches its maximum intensity [Stevenson, 1979]. Nevertheless, the recorded maximum of 57°C is markedly higher than expected, which could be related to direct solar radiation (Figure 42) combined with the heat-retaining properties of the roof materials.

On the other hand, the decrease in temperatures during WEEK 11 and the abnormally low readings in WEEK 12 may be linked to seasonal changes, with the former signifying the beginning of fall [Hillel, 2014]. The substantial decrease in temperature during WEEK 12 could potentially be attributed to an atypical meteorological occurrence, such as an untimely frost.

The WEEK 6 data indicate a significant temperature variance, possibly caused by unexpected meteorological circumstances such as occasional cloud cover or instances of precipitation [Van Bavel and Hillel, 1976]. By the end of October, the stability seen in WEEK 13 indicates that the green roof system has achieved a level of balance, possibly indicating that the vegetation has adapted to the dropping temperatures.

The elevated median values of downward shortwave radiation during WEEKS 1 and 2 can be explained to the summer conditions, characterized by extended daylight hours and an increased sun angle, which leads to a higher flow of solar energy reaching the roof [Hillel, 2014]. The presence of slightly negative values in WEEK 7 for shortwave radiation may suggest potential data recording anomalies, electronic noise or slight shift in calibrtion [Stevenson, 1979].

The downward net radiation pattern exhibits noticeable contrasts, particularly in WEEK 2 where there is a prominent peak that may suggest a week characterized by extraordinary sun exposure and low cloud interference [Van Bavel and Hillel, 1976]. The net radiation experienced a progressive decline from WEEK 1 to WEEK 11, which can be attributed to the transition towards fall. This transition is marked by a drop in solar elevation and daylight length, resulting in lower solar heating.

Temperatures of bare soil and area with vegetation in relation to subsurface substrate temperatures and air temperatures in 2 m and 5 cm and total rain

The temperature and precipitation data obtained from the green roof for a thirteen-week duration show intricate correlations between weather conditions and the thermal characteristics of the various components of the roof (Figure 43).

In WEEK 3, the temperatures of the part with vegetation and bare soil on the green roof reached their highest point. This might be attributed to various variables, including intense sunlight and no rainfall (Figure 44), as indicated by the reduced amount of rain in the previous WEEK 2. This may have resulted in increased heat absorption by the roofing materials [Hillel, 2003, Hillel, 2014]. The notable changes in temperature throughout WEEK 6, particularly in the bare soil, could be attributed to periodic weather patterns or potentially the beginning of plant growth or changes in soil moisture that impact the thermal characteristics of the soil [Hillel, 2003].

WEEK 12's extreme temperature drop, with outliers reaching as low as -6°C, could be associated with an unexpected weather event like a cold snap, which, while affecting the bare soil layer most severely, also impacted the vegetated areas and the temperatures above the roof, illustrating the green roof's vulnerability to abrupt climatic changes [Berardi et al., 2014]. The continuous elevation in temperatures observed in bare soil, as opposed to vegetated regions, across the whole study period may suggest that vegetation provides a cooling influence, while bare soil areas are more susceptible to direct sunlight and lack insulation [Hillel, 2003].

The continuously lower temperatures recorded 10 weeks below the height of 2 meters above the green roof indicate that the air above the roof may be cooler as a result of the roof's insulate capabilities or the evapotranspiration from the vegetation [Hillel, 2003]. The reversal of this tendency, which occurs in WEEK 11, can be attributed to the changing seasons. As winter approaches, the air temperature decreases, causing the temperature above the roof to surpass that of the surface. Yet, the green roof keeps some of its residual warmth [Stevenson, 1979].

The precipitation pattern, characterized by a sudden increase in WEEK 1 followed by a notable decline, especially in WEEK 3, and subsequent rises in WEEKS 2 and 4, indicates the fluctuating effect of rainfall on the temperature dynamics of the green roof. The roof may have become fully saturated by the highest amount of rainfall in WEEK 1, which impacted its ability to regulate temperature. Additionally, the lack of rainfall during WEEK 3 may have caused higher temperatures as there was less evaporative cooling [Hillel, 2014].

Comparison of measured temperatures on bare soil and area with vegetation

The scatter plots provided (Figure 45-48) offer a multi-dimensional view of the green roof's microclimate, defining the interactions between bare soil, vegetation, and atmospheric temperatures under varying solar radiation conditions. Each plot represents one particular aspect of the thermal dynamics of the green roof with a third variable to indicate either air temperature or radiation.

The continuous placement of data points below the diagonal line in the plots indicates that vegetated regions generally exhibit lower temperatures compared to bare soil. This is likely related to the cooling impact of transpiration and shading. This cooling effect seems more prominent at a moderate soil temperatures and decreases as soil temperatures rise demonstrating the limits of plant cooling under intense heat conditions.

Week-specific variations indicate that during WEEK 1, which is characterized by the greatest median soil temperatures, the cooling impact of vegetation remains apparent, indicating strong plant growth. By the WEEK 3, despite the high soil temperatures indicating strong solar heat, the vegetation appears to provide some cooling, although to a lesser extent, it is also effected by zero rainfall. This is evident from the wider range of air temperatures observed above the green roof, as indicated by the spread of data points. In WEEK 6, the soil temperatures were cooler, resulting in reduced variation in vegetation temperatures. This suggests that the green roof had a consistent and efficient cooling impact. WEEK 13, with its lower soil temperature range, indicates a consistent cooling effect across the vegetation, which might be attributed to the seasonal changes as the system transitions into a cooler period.

In terms of radiation, the plots demonstrate that bare soil and vegetation temperatures correlate with lower net and upward shortwave radiation levels. These findings indicate that the vegetation's cooling impact is most effective when radiation levels are lower, potentially because the plants experience less stress and can utilize moisture more efficiently for transpiration. As radiation levels rise, both soil and vegetation temperatures increase. However, vegetation remains relatively cooler, highlighting its function in regulating a microclimate.

The distribution of data points in relation to changes in air temperature further supports the concept that the green roof's temperature regulation is not fixed but dynamically responds to both the daily and seasonal shifts in weather patterns. The denser concentration of data points at higher temperatures during periods of increasing air temperature suggests that the green roof's cooling capacity is challenged during hotter periods, which could have implications for the design and management of green roofs in urban environments.

Simple model of behaviour of temperatures on bare soil

The graphical data (Figures 49 - 52) demonstrates the thermal behavior of bare soil on an experimental green roof. Across the different weeks, with varying conditions such as high rainfall in WEEK 1, no rainfall in WEEK 6, highest temperatures in WEEK 3, and lowest temperatures in WEEK 13, we observe some consistent trends along with specific variations in the model's ability to predict soil surface temperature.

The cyclic nature of both the modeled and measured temperatures is evident in all weeks, aligning with the daily temperature cycle of warming during the day and cooling at night. The cyclicity observed suggests that the model accurately represents the daily thermal patterns caused by solar heating and nighttime radiative cooling.

Nevertheless, the efficacy of the model varies depending on the different temperature circumstances of each week. During the first week, the model exhibits a tendency to overestimate daytime temperatures and underestimate nighttime temperatures. This discrepancy may be attributed to the significant moisture content caused by rainfall, which affects the heat capacity and thermal conductivity of the soil. It is possible that the model does not fully consider these factors. Conversely, in WEEK 6 when there was no rainfall, the disparities between the predicted and measured temperatures are less, indicating that the model is more precise in dealing with arid conditions.

During WEEK 3, the model has difficulties in accurately forecasting the higher temperatures. This may be attributed to the varying reactions of soil qualities to overbearing temperatures, which are inadequately reflected in the model. In contrast, during WEEK 13, when the temperatures were at their lowest, the model once again appears to inaccurately predict how the soil will react to cold conditions. It overestimates the soil temperature during the coldest periods and underestimates the cooling that occurs at night.

The similarities in the model's performance across all weeks are its general ability to replicate the shape of the temperature curve and its cyclical pattern, while the differences lie in its precise prediction of temperature extremes. This phenomenon can be connected to the complex interaction of soil characteristics, ambient factors, and the dynamics of solar radiation, which create difficulties in summarizing within a single model. The continuous underestimating or overestimation of maximum temperatures indicates that the model may require improvement in its depiction of the thermal characteristics of the soil and its handling of factors such as solar radiation and humidity, particularly during atypical weather conditions.

The model's performance is consistent under normal conditions, but it needs improvement in incorporating extreme weather factors. It should consider intricate soil moisture dynamics and diverse reactions during extreme weather events. The study [Hong and Utzinger, 2021] revealed discrepancies between the derived model and observed components, often overestimating during daylight and underestimated at midnight.

7 Conclusion

This thesis aimed to investigate the dynamic thermal regime of an experimental green roof, specifically examining the surface temperature and its relationship with different environmental conditions.

The laboratory findings of this study highlight the importance of sensor selection for monitoring green roof temperatures. The stainless steel probe responded quickly to temperature changes, proving advantageous for tracking the dynamic conditions of green roofs. The aluminum plate-equipped sensor did not accurately reflect the soil's surface temperatures, particularly in frozen conditions. Therefore the experimental readings on green roof were made with thin stainless steel probe during the thirteen-week observation period.

The comparison of temperatures between bare soil and vegetated regions demonstrated that vegetation provides a quantifiable cooling influence. During periods of high temperatures, the vegetated region exhibits temperatures that are up to 5°C lower than those observed on bare soil. Conversely, in cold weather, the temperature difference between the vegetated area and bare soil is only 1°C or less. This shows that Sedum spp. vegetation significantly reduce surface temperature of the roof. The continuous cooling effect exerted by vegetation across various weeks highlights the potential of green roofs to protect the building from high roof surface temperature.

The study showed that peak surface temperatures were almost constantly higher than subsurface temperatures through out the day time. In extreme temperatures, there was up to 10°C difference with the surface temperature at the bare soil. Yet, in the last week of October, the subsurface temperature was equal to the temperature on bare soil and even exceeded the temperature on the vegetated area. This phenomenon may be explained by a decrease in evapotranspiration rates as plants prepare for dormancy.

Even without extensive parameter optimization, the study noted that simulated soil temperatures, although generally consistent with the course of actual measurements, showed differences during periods of rapid temperature fluctuations or extreme weather conditions. During periods characterized by the most heavy rainfall and coldest temperatures, the model significantly overestimated the real temperature, particularly during daylight hours. Conversely, during weeks with no precipitation and the most elevated temperatures, the model exhibited a modest underestimation of the recorded daytime temperature. The model's overestimation occurred throughout the night interval, specifically in the week without rainfall and during the coldest week. This highlights the importance of improving prediction models to account for the complex responses of green roof systems to different external factors.

For future research, it would be beneficial to extend the duration of ongoing monitoring to capture a full annual cycle, exploring the impact of diverse meteorological conditions on green roof performance. In addition, the improvement of temperature models could improve our knowledge of the thermal dynamics of green roofs, eventually helping in the creation of more efficient green infrastructure in urban planning.

References

[zel, 2023] (2023). Zelená střecha roku. https://www.zelenastrecharoku.cz. Accessed: 2024-01-14.

[ACRE, 2021] ACRE, s. (2021). Etiketa.

[Aniley et al., 2017] Aniley, A. A., Kumar, N., and Kumar, A. (2017). Soil temperature sensors in agriculture and the role of nanomaterials in temperature sensors preparation. *Int. J. Eng. Manuf. Sci*, 7(2):2249–3115.

[Asshoff et al., 2006] Asshoff, R., Zotz, G., and Koerner, C. (2006). Growth and phenology of mature temperate forest trees in elevated co2. *Global Change Biology*, 12(5):848–861.

[Berardi et al., 2014] Berardi, U., GhaffarianHoseini, A., and GhaffarianHoseini, A. (2014). State-of-the-art analysis of the environmental benefits of green roofs. *Applied energy*, 115:411–428.

[Campbell Scientific, 2022] Campbell Scientific (2022). *Product manual - 109 Temperature Probe*. Accessed: 11-01-2024.

[Campbell Scientific, 2024] Campbell Scientific (2024). 109ss: Stainless-steel temperature probe for harsh environments. https://www.campbellsci.eu/109ss. Accessed: [11-01-2024].

[Campbell Scientific, nd] Campbell Scientific (n.d.). Photograph of the 109 temperature probe. https://campbellsci-res.cloudinary.com/image/upload/c_limit,f_auto,w_500,h_500/320.png. Accessed: [11-01-2024].

[Davey, 2023] Davey, R. (2023). Understanding the functionality and working of infrared sensors. [Online; accessed 10-January-2024].

[De Vries, 1952] De Vries, D. (1952). The thermal conductivity of soil. *Wageningen, Meded. Landbouwhogesch*, 52:1–73.

[De Vries and van Wijk, 1963] De Vries, D. and van Wijk, W.R., e. (1963). Thermal properties of soils. *Physics of the Plant Environment*.

[Doe, 2024] Doe, J. (2024). Innovative thermal dynamics. YouTube video. https://www.youtube.com/watch?v=xzQZcH40Umc.

[Edwards, 2023] Edwards, E. (2023). Types of noncontact sensors. [Online; accessed 10-January-2024].

[EnnoLogic, 2023] EnnoLogic (2023). et450c thermal imager with wifi. [Online; accessed 10-January-2024].

[Fallis, 2013] Fallis, A. (2013). *Handbook of Modern Sensors*. Publisher Name, 3rd edition.

[Feteira, 2009] Feteira, A. (2009). Negative temperature coefficient resistance (ntcr) ceramic thermistors: An industrial perspective. *Journal of the American Ceramic Society*, 92(5):967–983.

[Fioretti et al., 2010] Fioretti, R., Palla, A., Lanza, L. G., and Principi, P. (2010). Green roof energy and water related performance in the mediterranean climate. *Building and environment*, 45(8):1890–1904.

[Food and Agriculture Organization of the United Nations, 2024] Food and Agriculture Organization of the United Nations (2024). Agricultural landscape. Accessed: 2024-01-10.

[Fortin, 1993] Fortin, M.-C. (1993). Soil temperature, soil water, and no-till corn development following in-row residue removal. *Agronomy Journal*, 85(3):571–576.

[Gill, 2023] Gill, L. (2023). Comparing contact and non-contact temperature sensors. [Online; accessed 10-January-2024].

[Graser and Van Bavel, 1982] Graser, E. and Van Bavel, C. (1982). The effect of soil moisture upon soil albedo. *Agricultural Meteorology*, 27(1-2):17–26.

[Halim, 2017] Halim, A. A. A. (2017). Integrated circuit (ic) temperature sensor. [Online; accessed 11-01-2024].

[Ham and Senock, 1992] Ham, J. M. and Senock, R. (1992). On the measurement of soil surface temperature. *Soil Science Society of America Journal*, 56(2):370–377.

[Hillel, 2003] Hillel, D. (2003). *Introduction to environmental soil physics*. Elsevier.

[Hillel, 2014] Hillel, D. (2014). *Environmental soil physics: fundamentals, applications, and environmental considerations*. Elsevier Science Amsterdam, The Netherlands.

[Hong and Utzinger, 2021] Hong, J. and Utzinger, D. M. (2021). Reducing heat island effect: a mathematical model of green roof design. In *Building Simulation 2021*, volume 17, pages 1279–1286. IBPSA.

[Horton and Ochsner, 2011] Horton, R. and Ochsner, T. (2011). Soil thermal regime. *Handbook of Soil Sciences, 2nd ed.; Huang, PM, Li, Y., Summer, ME, Eds*, pages 9–23.

[Jackson et al., 1974] Jackson, R. D., Reginato, R., Kimball, B., and Nakayama, F. (1974). Diurnal soil-water evaporation: Comparison of measured and calculated soil-water fluxes. *Soil Science Society of America Journal*, 38(6):861–866.

[Jakar, 2023] Jakar (2023). *Manual of SA1-RTD Self-Adhesive RTD Sensor*. Accessed: 2024-01-11.

[Johnston, 2020] Johnston, H. (2020). Thermal physics notes. http://www.physics.usyd.edu.au/~helenj/Thermal/PDF/thermal4.pdf. Accessed: 2024-01-10.

[Kuphaldt, 2023] Kuphaldt, T. R. (2023). Non-contact temperature sensors. [Online; accessed 10-January-2024].

[LambdaGeeks, 2023] LambdaGeeks (2023). Infrared temperature sensor. [Online; accessed 10-January-2024].

[Liapor, 2024] Liapor (2024). Co je liapor? [what is liapor?].

[Mapy.cz, 2024] Mapy.cz (2024). Mapy.cz - [-].

[MISUMI, 2024] MISUMI (2024). Temperature sensor. https://vn.misumi-ec.com/linked/material/fs/SWS1/PHOTO/223000505861_001.jpg. Accessed: 2024-01-14.

[Mukhopadhyay, 2022] Mukhopadhyay, B. (2022). What are the different types of temperature sensors? Figure available at: https://i0.wp.com/nexthermal.com/wp-content/uploads/Sensors-Chart.png?w=1353&ssl=1. Accessed: 2024-01-10.

[NASA Earthdata, 2023] NASA Earthdata (2023). Air mass density. https://www.earthdata.nasa.gov/topics/atmosphere/atmospheric-pressure/air-mass-density. Accessed: 2024-01-14.

[Ni An, 2017] Ni An, Sahar Hemmati, Y.-J. C. (2017). Assessment of the methods for determining net radiation on different time-scales of meteorological variables. https://www.researchgate.net/publication/312558412_Assessment_of_the_methods_for_determining_net_radiation_on_different_time-scales_of_meteorological_variables/figures?lo=1. Accessed: 2024-01-14.

[Niachou et al., 2001] Niachou, A., Papakonstantinou, K., Santamouris, M., Tsangrassoulis, A., and Mihalakakou, G. (2001). Analysis of the green roof thermal properties and investigation of its energy performance. *Energy and buildings*, 33(7):719–729.

[Oberndorfer et al., 2007] Oberndorfer, E., Lundholm, J., Bass, B., Coffman, R. R., Doshi, H., Dunnett, N., Gaffin, S., Köhler, M., Liu, K. K., and Rowe, B. (2007). Green roofs as urban ecosystems: ecological structures, functions, and services. *BioScience*, 57(10):823–833.

[Omega Engineering, 2023] Omega Engineering, I. (2023). Integrated circuit sensors. [Online; accessed 11-January-2024].

[Pauleit et al., 2019] Pauleit, S., Ambrose-Oji, B., Andersson, E., Anton, B., Buijs, A., Haase, D., Elands, B., Hansen, R., Kowarik, I., Kronenberg, J., et al. (2019). Advancing urban green infrastructure in europe: Outcomes and reflections from the green surge project. *Urban forestry & urban greening*, 40:4–16.

[Perez, 2019] Perez, H. M. (2019). Year 2017 emissions inventory study. https://www.researchgate.net/publication/337438060_Year_2017_Emissions_Inventory_Study/figures?lo=1. Accessed: 2024-01-14.

[Ramos et al., 2012] Ramos, M., De Pablo, M., Sebastian, E., Armiens, C., and Gómez-Elvira, J. (2012). Temperature gradient distribution in permafrost active layer, using a prototype of the ground temperature sensor (rems-msl) on deception island (antarctica). *Cold Regions Science and Technology*, 72:23–32.

[Rugged Monitoring, 2019] Rugged Monitoring (2019). How fiber optic temperature sensor works. https://issuu.com/ruggedmonitoring/docs/how_fiber_optic_temperature_sensor_works.pptx. Accessed: 2024-01-14.

[Sadler, 1984] Sadler, G. W. (1984). Global longwave radiation at edmonton, alberta. In *Energy Developments: New Forms, Renewables, Conservation*, pages 397–402. Elsevier.

[Sailor, 2008] Sailor, D. J. (2008). A green roof model for building energy simulation programs. *Energy and buildings*, 40(8):1466–1478.

[Santamouris, 2014] Santamouris, M. (2014). On the energy impact of urban heat island and global warming on buildings. *Energy and Buildings*, 82:100–113.

[Sellers, 1965] Sellers, W. (1965). Illinois.

[Sensors, 2023] Sensors, P. (2023). Rtd sensor with metal pocket. [Online; accessed 11-01-2024].

[Sněhota et al., 2021] Sněhota, M., Hanzlíková, J., Sobotková, M., and Moravcik, P. (2021). Water and thermal regime of extensive green roof test beds planted with sedum cuttings and sedum carpets. *Journal of Soils and Sediments*, 21:2089–2101.

[Sněhota et al., nd] Sněhota, M., Jelínková, V., Šácha, J., Bareš, V., and Vogel, T. (n.d.). MeteorologickÁ mĚŘenÍ v okolÍ budovy uceeb. *Energeticky efektivní budovy 2015, ročenka výzkumu a vývoje v UCEEB ČVUT Buštěhrad*.

[Solutions, 2023] Solutions, O. (2023). Otg-pm photo. [Online; accessed 10-January-2024].

[Stevenson, 1979] Stevenson, R. (1979). Heat transfer processes for the thermal energy balance of organisms. physical processes in terrestrial and aquatic ecosystems, transport processes.

[Systems, 2023] Systems, C. D. (2023). Thermistor function and roles. [Online; accessed 11-01-2024].

[Thermo-Probes, 2023] Thermo-Probes, I. (2023). Thermocouples. [Online; accessed 11-01-2024].

[Tillman, 2015] Tillman, P. B. (2015). Growth performance of ross × ross 708 male broilers fed various digestible arg (darg)-to-digestible lys (dlys) ratios from 28 to 42 d of age during a constant, elevated environmental temperature regimen. Accessed: 2024-01-10.

[Tzoulas et al., 2007] Tzoulas, K., Korpela, K., Venn, S., Yli-Pelkonen, V., Kaźmierczak, A., Niemela, J., and James, P. (2007). Promoting ecosystem and human health in urban areas using green infrastructure: A literature review. *Landscape and urban planning*, 81(3):167–178.

[Van Bavel and Hillel, 1976] Van Bavel, C. and Hillel, D. (1976). Calculating potential and actual evaporation from a bare soil surface by simulation of concurrent flow of water and heat. *Agricultural Meteorology*, 17(6):453–476.

[Votrubova et al., 2012] Votrubova, J., Dohnal, M., Vogel, T., and Tesař, M. (2012). On parameterization of heat conduction in coupled soil water and heat flow modelling. *Soil and Water Research*, 7(4):125–137.

[Wikipedia, 2024] Wikipedia (2024). Standard atmosphere (unit). `https://en.wikipedia.org/wiki/Standard_atmosphere_(unit)`. Accessed: 2024-01-14.

[Woolf, 2023] Woolf, P. (2023). Temperature sensors. [Online; accessed 11-January-2024].

[Wuest, 2013] Wuest, S. (2013). An array for measuring detailed soil temperature profiles. *Soil Science Society of America Journal*, 77(2):427–431.

[Young et al., 2014] Young, H. D., Freedman, R. A., and Ford, A. L. (2014). *University physics with modern physics*. Pearson New York.

[Yu et al., 2008] Yu, J., Yang, C., and Tian, L. (2008). Low-energy envelope design of residential building in hot summer and cold winter zone in china. *Energy and Buildings*, 40(8):1536–1546.

8 Appendix A - Matlab script

% Define constants and inputs
xs = 0.45 %volume fraction of solids odhad xs = 0.4500
lambda = 2.43* 10^6; $\%J/kgLatentheatofvaporization$,
alfa$_s olar$ = 0.85$\%odhad$
alfa$_s olar$ = 0.8500
eta$_s oil$ = 0.98;
eta$_s oilsat$ = 0.99;
eta$_s oildry$ = 0.98;
T$_s ky$ = 270$\%odhadjetrebapocitatT_s ky = 270$
E$_s oil$ = 0.01; $\%Soilevaporationrateinkg/m^2/s$
k$_e$ = 0.432; $\%Effectivethermalconductivityin W/m/K$
%temp = 300; % Soil temperature in K
%sandpercent = 50; % Sand percentage in %
%claypercent = 20; % Clay percentage in %
%specificgravity = 2.65; % Specific gravity of soil
% vwc = 0.2; % Volumetric water content of soil
d= 0.03;
ro$_a ir$ = 1.293$\%airdensitykgm3$
ro$_a ir$ = 1.2930
Pa = 101325
C = 0.0015

% Import data for BS from Excel
BS$_d ata = xlsread('BS.xlsx'); \%Replace'BS.xlsx'withyouractualExcelfilename$

% Import data for I$_s olarfromExcel$
I$_s olar_d ata = xlsread('I_s olar.xlsx'); \%Replace'I_s olar.xlsx'withyouractualExcelfile$

% Import data for T$_a irfromExcel$
T$_a ir_d ata = xlsread('T_a ir.xlsx'); \%Replace'T_a ir.xlsx'withyouractualExcelfilename$

% Import data for V from Excel
V$_d ata = xlsread('V.xlsx'); \%Replace'V.xlsx'withyouractualExcelfilename$

% Import data for T$_s oilfromExcel$
T$_s oil_d ata = xlsread('T_s oil.xlsx'); \%Replace'T_s oil.xlsx'withyouractualExcelfilename$

% Check if the data has been imported correctly (optional) disp('T$_s oildata$:');
% Perform calculations or operations using these variables as needed
% For example, you can calculate something based on these variables:
% result = some$_f unction(I_s olar_d ata, T_a ir_d ata, V_d ata)$;

```
    % Save the variables to a MAT file for future use
    save('variables_data.mat','I_solar_data','T_air_data','V_data');%Saveallvariablestoaf
    % I_solar = 800;%SolarradiationinW/m^2
    % T_air = 300;%AirtemperatureinK
    % V = 2; % wind speed will be variated
    % T_d = 290;%DeepsoiltemperatureinK
    % T_soil = 293;%soiltemperature
    % Define frequency range
    % fc = linspace(1e6, 1e9, 100); % Frequency in Hz
    tc = linspace(0, 10079, 10080); % Time steps

% Initialize soil surface temperature vector
    T_surf = zeros(size(tc));

% Initialize soil evaporation rate vector
    E_soil = zeros(size(tc));

    % Other constants and parameters % ...
    % Loop through time steps to calculate soil surface temperature
    for t = 1:length(tc)
T_AVG = (T_air_data(t) + T_sky)/2;%Calculateaveragetemperatureh_c =
2.8 + 3.0 * V_data(t);%Calculateconvectiveheattransfercoefficient
%Calculatesoilevaporationratebasedongivenequation E_soil(t) = ro_air*C*V_data(t)*
(0.622/Pa)*0.61078*...(exp(17.27*T_soil_data(t)/(T_soil_data(t)+237.3)) - exp(17.27*
T_air_data(t)/(
%Calculatesoilsurfacetemperature T_surf(t) = (I_solar_data(t) * alfa_solar + 4 *
eta_soil * sigma * ((T_AVG)^3) * T_sky + ..h_c * T_air_data(t) + (k_e/d) * T_soil_data(t) -
lambda * E_soil(t))/...(h_c + 4 * eta_soil * sigma * ((T_AVG)^3) + (k_e/d));

    end % ... % ... % ...
% Load BS data
    BS = importdata('BS.xlsx');
    % Plot soil surface temperature and BS data in the same figure
    figure;
    % Plot soil surface temperature vs time in Celsius
    plot(tc, T_surf-273.15,'b','LineWidth',1.5);%SoilsurfacetemperatureinCelsius
    hold on; % Hold the current plot
    % Plot BS data vs time
    plot(tc, BS, 'r', 'LineWidth', 1.5); % BS data
    hold off; % Release the hold
    % Limit the x-axis range to 10080 minutes
    xlim([0, 10080]);
    xlabel('Time (minutes)');
```

ylabel('Temperature (°C)');
legend('Modeled soil surface temperature (°C)', 'Measured soil surface temperature (°C)');
grid on;
% Assuming $T_surf and tc are vectors containing your data$
% Create a table with $T_surf and tc data$
$data_table = table(tc', T_surf', 'VariableNames', 'Time_minutes', 'T_surf_Celsius');$
% Define the filename for the Excel sheet
filename = '$T_surf_data_table.xlsx$';
% Write the table to an Excel file
writetable($data_table, filename$);
% ... (Previous code)
% Initialize sum of squares difference
$sum_squared_diff = 0;$
% Loop through time steps to calculate soil surface temperature
for t = 1:length(tc)
% ... (Your existing calculations within this loop)
% Calculate the difference between $T_surf and BS, and then square it$
$squared_diff = (T_surf(t)^2) - (BS_data(t)^2);$
% Add the squared difference to the sum
$sum_squared_diff = sum_squared_diff + squared_diff;$
end